

**ELECTROSTATIC FREE-FREE BEAM  
MICROELECTROMECHANICAL RESONATOR**

by

Tianming Zhang

Submitted in partial fulfilment of the requirements  
for the degree of Master of Applied Science

at

Dalhousie University  
Halifax, Nova Scotia  
October 2012

© Copyright by Tianming Zhang, 2012

DALHOUSIE UNIVERSITY

DEPARTMENT OF ELECTRICAL AND COMPUTER ENGINEERING

The undersigned hereby certify that they have read and recommend to the Faculty of Graduate Studies for acceptance a thesis entitled “ELECTROSTATIC FREE-FREE BEAM MICROELECTROMECHANICAL RESONATOR” by Tianming Zhang in partial fulfilment of the requirements for the degree of Master of Applied Science.

Date: October 31, 2012

Supervisors:

---

---

Readers:

---

---

DALHOUSIE UNIVERSITY

DATE: October 31, 2012

AUTHOR: Tianming Zhang

TITLE: ELECTROSTATIC FREE-FREE BEAM  
MICROELECTROMECHANICAL RESONATOR

DEPARTMENT OR SCHOOL: Department of Electrical and Computer Engineering

DEGREE: MASC CONVOCATION: May YEAR: 2013

Permission is herewith granted to Dalhousie University to circulate and to have copied for non-commercial purposes, at its discretion, the above title upon the request of individuals or institutions. I understand that my thesis will be electronically available to the public.

The author reserves other publication rights, and neither the thesis nor extensive extracts from it may be printed or otherwise reproduced without the author's written permission.

The author attests that permission has been obtained for the use of any copyrighted material appearing in the thesis (other than the brief excerpts requiring only proper acknowledgement in scholarly writing), and that all such use is clearly acknowledged.

---

Signature of Author

To my parents Jun Zhang and Ping Zhou

## TABLE OF CONTENTS

LIST OF TABLES .....	vii
LIST OF FIGURES .....	viii
ABSTRACT .....	xi
LIST OF ABBREVIATIONS USED .....	xii
ACKNOWLEDGEMENTS .....	xiv
CHAPTER 1 INTRODUCTION .....	1
1.1 MEMS Definition .....	1
1.2 MEMS Resonator .....	2
1.2.1 Literature Review .....	3
1.2.2 Applications of MEMS Resonators .....	5
1.3 Motivations and Thesis Contribution .....	6
1.4 Thesis Outline .....	8
CHAPTER 2 MEMS FABRICATION PROCESS .....	9
2.1 MEMS Fabrication Techniques .....	9
2.2 Bulk Micromaching Process .....	9
2.3 Surface Micromachining Process .....	11
2.3.1 UW-MEMS Process .....	12
2.3.2 PolyMUMPs .....	15
2.4 MEMS Resonator Layout .....	17
2.5 Summary .....	18
CHAPTER 3 THE FREE-FREE BEAM MEMS RESONATOR .....	19
3.1 Resonator Structure and Operation .....	19
3.2 Mathematical Model .....	22
3.2.1 Resonant Frequency Design .....	22
3.2.2 Support Structure Design .....	25
3.2.3 Electromechanical Coupling .....	29
3.2.4 Control Voltage .....	33
3.3 Micro-Resonator Design Parameters .....	35
3.4 Small-Signal Electrical Equivalent Circuit .....	38
3.4.1 Mechanic to Electric Analogy .....	38

3.4.2	Equivalent Electrical Circuit.....	41
3.5	Summary .....	45
CHAPTER 4	FINITE ELEMENT ANALYSIS .....	46
4.1	Introduction to FEA.....	46
4.2	Analysis for UW-MEMS Resonator.....	47
4.2.1	Modal Analysis .....	47
4.2.2	Static Analysis.....	50
4.2.3	Dynamic Response Analysis.....	52
4.3	Analysis for PolyMUMPs Resonator.....	54
4.4	Summary .....	58
CHAPTER 5	EXPERIMENTAL IMPLEMENTATION .....	59
5.1	Static and Dynamic Testing of UW-MEMS Resonator.....	59
5.1.1	Experimental Setup.....	60
5.1.2	Static Measurement.....	61
5.1.3	Dynamic Testing .....	63
5.2	Electrical Testing of UW-MEMS Resonators .....	65
5.3	Results and Analysis.....	68
5.3.1	Resonance Frequency .....	68
5.3.2	Quality Factor .....	69
5.4	Summary .....	70
CHAPTER 6	CONCLUSIONS AND FUTURE WORK.....	71
6.1	Conclusions .....	71
6.2	Future Work.....	72
BIBLIOGRAPHY	.....	73
APPENDIX A	COMSOL Multiphysics Steps .....	76
APPENDIX B	PolyMUMPs Static Measurements .....	80

## LIST OF TABLES

Table 1: Materials, thickness and layer descriptions of UW-MEMS process [21] .....	15
Table 2: PolyMUMPs layers and their properties [20].....	16
Table 3: Mode shape for a vibration beam in various boundary conditions [28].....	23
Table 4: The torsion constant parameter with different side ratios .....	28
Table 5: Free-free beam resonator design parameters in the UW-MEMS process .....	36
Table 6: Free-free beam resonator design parameters in PolyMUMPs.....	37
Table 7: Corresponding elements between mechanical and electrical domain .....	41
Table 8: Equivalent electrical lumped parameters of UW-MEMS resonator.....	43
Table 9: Equivalent electrical lumped parameters of PolyMUMPs resonator .....	43
Table 10: Material properties used in FEA for UW-MEMS resonator .....	47
Table 11: Material properties used in FEA for PolyMUMPs resonator .....	55
Table 12: Comparison between theoretical, simulation and experimental results.....	68
Table 13: Comparison of quality factor between FEA and experimental results.....	69

## LIST OF FIGURES

Figure 1. 1:	(a) Structure of a folded-beam comb-drive micro-resonator, (b) Measured transfer function for the fabricated resonator [6].	4
Figure 1. 2:	(a) SEM of a clamped–clamped beam resonator, (b) Frequency characteristic for an 8.5 MHz resonator [7].	4
Figure 1. 3:	(a) SEM of a free-free beam resonator, (b) Measured frequency spectrum for a 50.35 MHz resonator [8].	4
Figure 1. 4:	Schematic of a fabricated contour mode disk resonator [9].	5
Figure 1. 5:	(a) Free-free beam resonator, (b) Package resonator, (c) Resonator and ASIC, (d) QFN packaged oscillator [13].	6
Figure 2. 1:	Various bulk micromachining structures [1]	10
Figure 2. 2:	Example of Surface Micromachining Process	12
Figure 2. 3:	Deposition of Chromium and first dielectric layers on the substrate	13
Figure 2. 4:	Deposition and patterning of first gold layer and second dielectric layer	13
Figure 2. 5:	Sacrificial layer deposition and anchor holes, dimple patterning	14
Figure 2. 6:	Final structural layer deposition and complete structure after releasing	14
Figure 2. 7:	PolyMUMPs layers and their thickness	16
Figure 2. 8:	3D layout of UW-MEMS resonator in L-edit	17
Figure 3. 1:	Perspective view of a free-free beam resonator with setup configuration	19
Figure 3. 2:	Overhead view, indicating dimensions of the resonator structure	20
Figure 3. 3:	(a) Cross section view of a structure after fabrication and before operation, (b) After application of a large enough DC voltage to attract dimples down.	21
Figure 3. 4:	Plot for resonant frequency against beam length for two processes	25
Figure 3. 5:	Plot of the normalized fundamental mode shape for a 100 $\mu$ m beam	26
Figure 3. 6:	Quarter-wavelength torsional beam with B side anchoring and equivalent acoustic network showing zero impedance at port A with port B open	27

Figure 3. 7:	A simple mechanical system with mass, spring and damper.....	29
Figure 3. 8:	Cross section schematic of a free-free beam resonator, indicating key variables used in formulations .....	31
Figure 3. 9:	Value of $Ke / K$ against the applied DC voltage bias .....	35
Figure 3.10:	Photograph of a fabricated 100 $\mu\text{m}$ free-free beam resonator .....	38
Figure 3.11:	Signal and energy transformation flow graph .....	39
Figure 3.12:	An ideal series RLC electrical resonant circuit .....	40
Figure 3.13:	Equivalent lumped circuit for a single resonator .....	42
Figure 3.14:	Schematic of an equivalent lumped circuit in ADS.....	43
Figure 3.15:	Frequency characteristic of the 263.6. kHz UW-MEMS resonator.....	44
Figure 3.16:	Frequency characteristic of the 7 MHz PolyMUMPs resonator.....	44
Figure 4. 1:	Modal analysis of the first three harmonic resonance modes of the FF-beam: (a) First mode with frequency of 263.5 kHz, (b) Second mode with frequency of 736 kHz, (b) Third mode with frequency of 1.456 MHz .....	49
Figure 4. 2:	Simulated curve of the first mode shape for a 100 $\mu\text{m}$ free-free beam ..	50
Figure 4. 3:	Electric potential field and contours in the gap between the grounded resonator and the biased driving electrode .....	51
Figure 4. 4:	Displacement of the resonator under DC bias of 25 V .....	51
Figure 4. 5:	Displacements of the UW-MEMS beam under different DC bias voltage.....	52
Figure 4. 6:	Dynamic response of the fundamental mode of the resonator.....	53
Figure 4. 7:	Resonance frequency shown against the applied DC voltage bias.....	54
Figure 4. 8:	Fundamental mode shape of a 49.4 $\mu\text{m}$ free-free beam with eigenfrequency of 7.01 MHz .....	55
Figure 4. 9:	Mode shape of the PolyMUMPs resonator with the support structures, the eigenfrequency of which is 7.03 MHz .....	56
Figure 4.10:	Displacements of the beam under different DC bias voltage .....	57
Figure 4.11:	Dynamic response of the 49.4 $\mu\text{m}$ beam PolyMUMPs resonator .....	57
Figure 5. 1:	Photograph of a UW-MEMS packaged chip .....	59
Figure 5. 2:	Photograph of the dynamic experimental setup: ① Veeco NT 9100 optical profiler, ② Packaged chip, ③ DC power supply, ④ AC signal generator, .....	60

Figure 5. 3:	3D view of the UW-MEMS resonator .....	61
Figure 5. 4:	2D surface profile along the length of the resonator .....	62
Figure 5. 5:	2D surface profile along the width of the resonator .....	62
Figure 5. 6:	2D surface profile along the width of the resonator under DC bias .....	63
Figure 5. 7:	Dynamic testing for resonance performance .....	64
Figure 5. 8:	Quality factor determination .....	64
Figure 5. 9:	Schematic diagram of the electrical testing .....	65
Figure 5.10:	Photograph of the electrical testing setup .....	66
Figure 5.11:	Measured data in electrical testing and plotted fitting curve .....	67
Figure B. 1:	2D surface profile along the length of the PolyMUMPs resonator.....	80
Figure B. 2:	2D surface profile along the width of the PolyMUMPs resonator .....	80
Figure B. 3:	X Profile of the PolyMUMPs resonator after applied voltage.....	81
Figure B. 4:	3D side view of the micro-resonator.....	81

## **ABSTRACT**

Several free-free beam micro-resonators are designed and fabricated using two commercially available surface micromachining processes, the UW-MEMS process and PolyMUMPs. Theoretical derivations of the design parameters are presented and an electrical lumped behavior model is developed for a single resonator with direct mechanic-to-electric analogy. A finite-element analysis (FEA) tool, the COMSOL Multiphysics 4.2a, is utilized to simulate the effects of the critical structural dimensions and electromechanical coupling. A variety of analyses, such as modal, static and dynamic responses are performed in FEA and the results are compared with the analytical solutions. The static and dynamic performances of the fabricated UW-MEMS resonators are tested using the Veeco NT-9100 In-Motion System. The electrical testing is carried out to obtain the frequency characteristics in electrical domain of the device. Measured data are compared with the analytical and simulation results. Discrepancies are discussed and analyzed.

## LIST OF ABBREVIATIONS USED

$C$	Capacitance
$E$	Young's modulus of elasticity
$F$	Electrostatic force
$G$	Shear modulus of elasticity
$I$	Bending moment of inertia
$J_s$	Polar moment of inertia of support beam
$L$	Inductance
$L_r$	Length of the resonator beam
$L_s$	Length of the support beam
$L_1$	Lower electrode edge location
$L_2$	Upper electrode edge location
$Q$	Quality factor
$R$	Resistance
$R_o$	Measurement load resistance
$T_r$	Thickness of the beam
$V_{dc}$	DC bias voltage
$V_{in}$	Input ac voltage
$V_{out}$	Output ac voltage developed across $R_o$
$V_{pull-in}$	Catastrophic pull-in voltage
$V_d$	Dimple-down voltage
$W_{(y)}$	Mode shape function
$W_r$	Width of the resonator beam
$W_e$	Width of the electrode
$W_s$	Width of the support beam
$c$	Damping coefficient
$f_0$	Resonance frequency
$f$	Resonance frequency under DC bias
$g_0$	Initial gap
$g(y)$	Gap spacing at location $y$ along the beam length
$i$	AC current
$k_e$	Electrical stiffness arising from electromechanical coupling
$k_{(y)}$	Z-direction Equivalent stiffness of a resonator beam at location $y$ along beam length
$k_s$	Stiffness of the support beam
$k_{com}$	Combined stiffness of all support beams.
$m_{(y)}$	Equivalent mass of a resonator beam at location $y$ along its length
$v_{(y)}$	Velocity of beam at location $y$ along the length
$\eta$	Transformation coefficient
$Y$	Torsion constant

$\lambda$	Wavelength of the acoustic signal
$\omega$	Angular frequency
$\nu$	Poisson's ratio
$\epsilon_0$	Permittivity in vacuum ( $8.854 \times 10^{-12}$ F/m)
$\rho$	Density

## **ACKNOWLEDGEMENTS**

I would like to express my sincere gratitude to my supervisor Dr. Yuan Ma and co-supervisor Dr. Zhizhang (David) Chen for their helpful guidance, constant patience and encouragement throughout my graduate study. I would also like to thank Dr. Kamal El-Sankary and Dr. Williams J. Phillips for sitting on my supervisory committee.

To all my lab mates in the Advanced MEMS Lab, Hasan Imam and Sri Raghu, I appreciate the sharing of time, space and thoughts with them as well as their selfless supports and constructive advices on my research. And I want to thank all my friends whom I met in Halifax, especially Haoran Yu, Aidong Yang, Zichen Zhang, Dongming Han, Xiaou Mao, Chen Wei, Luyu Wang, for their kind help on my study and living here.

Last but not least, I would like to express my deepest appreciation to my parents. Their consistent love and support is my source of inspiration and makes all of this possible.

## **CHAPTER 1 INTRODUCTION**

This chapter introduces the definition of microelectromechanical system (MEMS), followed by the research background and the state-of-the-art of MEMS resonators. Motivations and thesis outline are given at the end of this chapter.

### **1.1 MEMS DEFINITION**

Microelectromechanical system, or MEMS, is a technology that in the most general form can be defined as micro-scale mechanical and electro-mechanical devices that are made by using the techniques of microfabrication [1]. The critical physical dimensions of MEMS structures vary from submicron to millimeters. Such devices are fabricated by employing a wide range of technologies similar to that for the integrated circuit process. They can integrate different functionalities across a variety of disciplines. Because of the significant advantages of its material properties, silicon (both single-crystal silicon and polycrystalline silicon) is commonly used for manufacturing MEMS devices [2]. New material such as polymers, metals and ceramics are being increasingly adopted in MEMS fabrication due to their advantageous combinations of material properties.

The most common MEMS elements are the micro-sensors and micro-actuators which are categorized as transducers. Sensor is a device that transforms energy from one form into another and provides a user with a detectable output. MEMS sensors may sense change of force, temperature, pressure, magnetic flux or other physical changes and convert them into an electrical signal or energy. The micro-actuator does the reverse things. It converts the electrical signal to mechanical signal. Commonly used

actuation schemes may include thermal deformation, electrostatic forces, electromagnetic forces [2].

Depending on their applications, MEMS can be classified into many different types, such as Bio-MEMS, RF-MEMS, Optical-MEMS, Energy and Power MEMS [3]. Some of them are now commercially available, like DLP projectors (Texas Instrument), pressure sensor, airbag accelerometer (Analog Device Inc.), ink-jet print heads (Hewlett-Packard) and resonator-based oscillator (Discera Inc.) etc.

## **1.2 MEMS RESONATOR**

Performance of an electronic system may depend highly on stability and accuracy of the frequency reference device it uses. However, our conventional clocks or frequency reference device are often too large and consume too much power to be implemented in today's wireless communication applications. For example, quartz crystals, surface acoustic wave (SAW) filters, and film bulk acoustic resonator (FBAR) are all off-chip components which must interface with transistor electronics at the board level, taking up a certain amount of board space [4]. Therefore, there is an increasing interest in designing on-chip IC compatible and low-power consumption resonators. Vibrating resonators produced by using micromachining fabrication process have been extensively investigated in recent years because of its advantages such as small size, light weight, good performance, high reliability and lower cost.

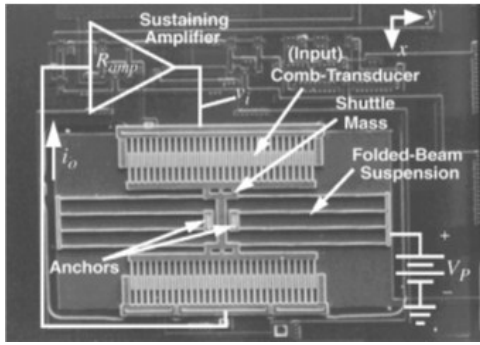
### 1.2.1 Literature Review

The earliest report about electro-mechanical resonators was presented in book [5]. It introduces design, modeling of mechanical resonators, and links them to electrical circuits. In 1997, the first MEMS resonator, the folded-beam comb-drive resonator, was fabricated and tested by Cao and T.-C.Nguyen at the University of Michigan, at Ann Arbor [6]. The structure as shown in Figure 1.1 was shown capable of electrostatically actuation of the silicon-based microfabricated resonator. The center frequency of the resonator is around 20 kHz with Qs of 20 to 130 in vacuum.

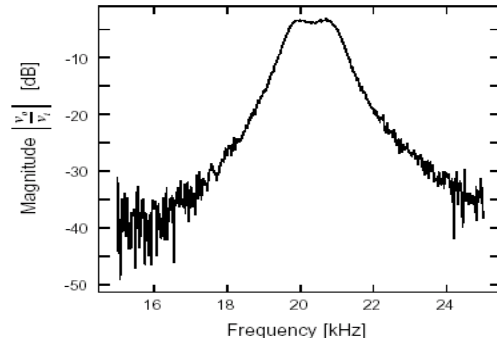
In 1999, a new high-Q High Frequency (HF) microelectromechanical filter was fabricated which consists of two clamped-clamped beam resonators coupled together by a soft coupling beam [7]. Each resonator is anchored at both ends and is tested up to 54.2 MHz with Q of 840 in vacuum (see Figure 1.2).

In 2000, free-free beam flexural-mode micromechanical resonators utilizing nonintrusive supports were demonstrated to achieve measured quality factor as high as 8000 at frequencies between 30 and 90 MHz. The resonators have the minimized anchor dissipation, achieving a higher quality factor than a clamped-clamped beam resonator at a high frequency range [8]. Figure 1.3 shows the schematic of a free-free beam with center frequency of 50.35 MHz.

Later in 2003, a laterally vibrating radial-contour mode disk resonator was developed at a frequency of 156 MHz with Q's as high as 9400 [9]. As depicted in Figure 1.4, it has two independent electrodes surrounding the vibrating disk in order to allow symmetric electrostatic excitations which in turn produce expansion and contraction of the disk along its radius. This result represents an important step toward reaching the frequencies required in wireless transceivers.

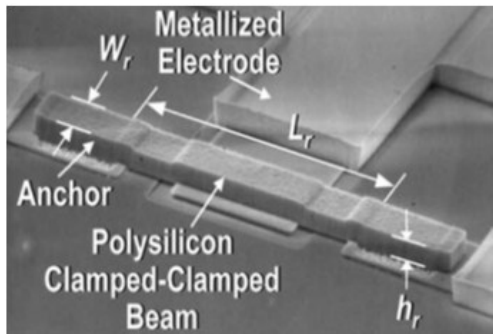


(a)

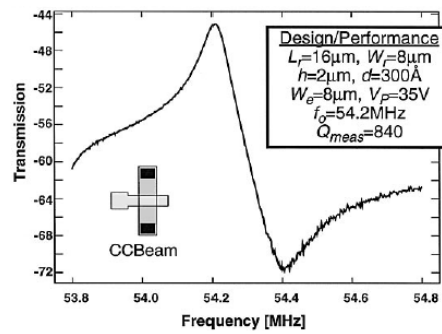


(b)

Figure 1. 1: (a) Structure of a folded-beam comb-drive micro-resonator, (b) measured transfer function of the fabricated resonator [6]

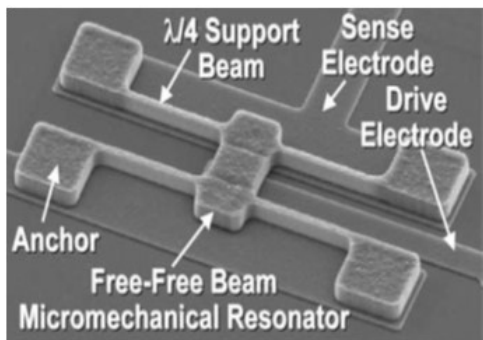


(a)

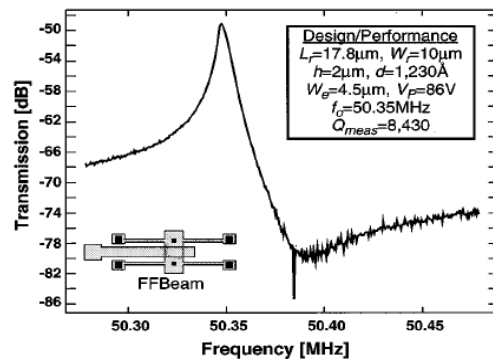


(b)

Figure 1. 2: (a) Structure of a clamped-clamped beam micromechanical resonator, (b) measured transmission in vacuum under a dc-bias voltage  $V_p = 10$  V and a drive voltage of  $v_i = 5$  mV [7]



(a)



(b)

Figure 1. 3: (a) Structure of a free-free beam polysilicon micromechanical resonator, (b) measured transmission for a 50.35 MHz resonator [8]

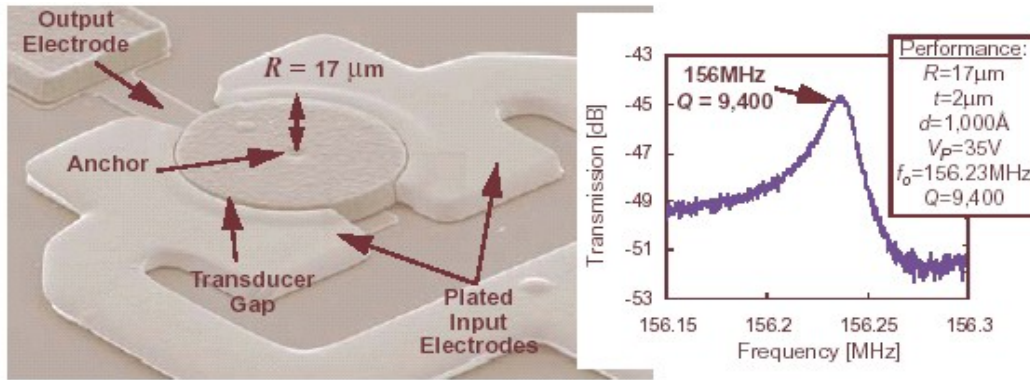


Figure 1. 4: Schematic of a fabricated 156 MHz contour mode micromechanical disk resonator with a measured frequency characteristic [9]

### 1.2.2 Applications of MEMS Resonators

MEMS resonators have come a long way and have a wide range of applications in different fields of engineering. Based on their functionality and applications, they can be divided into two major categories: mass MEMS sensors and RF-MEMS devices [10]. This thesis mainly focuses on the topic of RF-MEMS area, other applications will not be discussed.

Due to the functionality of frequency selection, MEMS resonators can be used as the core part of oscillators and band-pass filters in a RF front-end [11]. MEMS-based oscillators operating at frequencies below 100 MHz are already commercially available. One of the most notable examples is the products developed by Discera Inc. Figure 1.5 in below presents the procedure from a single resonator to a final oscillator product.

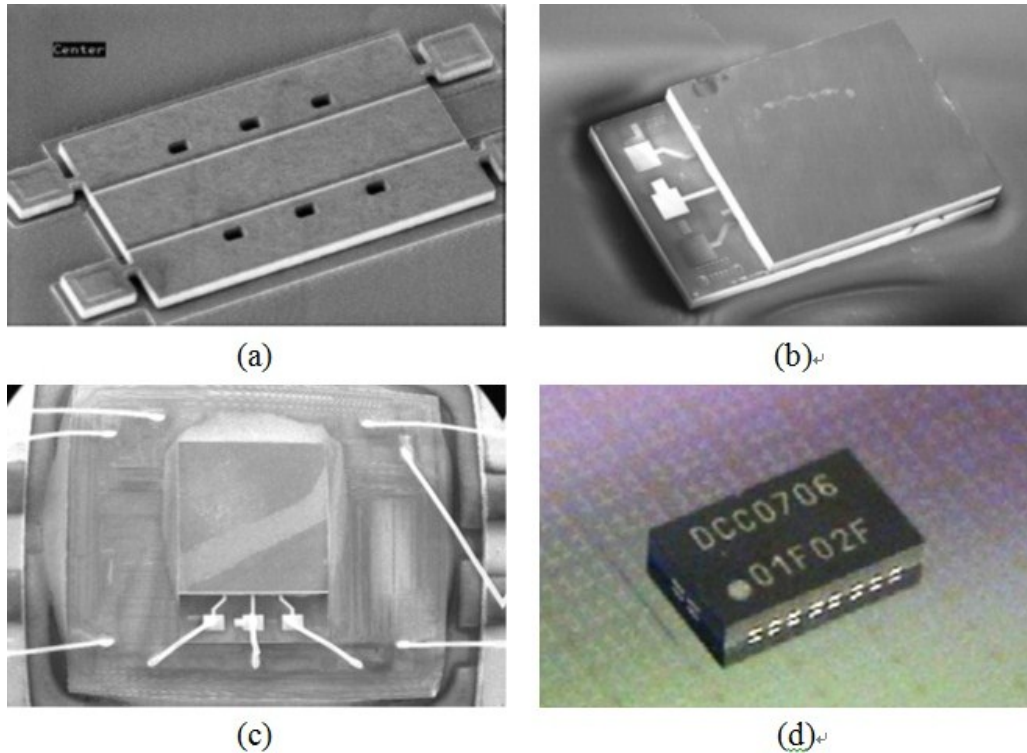


Figure 1. 5: (a) A free-free beam resonator, (b) Package resonator, (c) Resonator and ASIC, (d) QFN packaged oscillator [13]

Compared to quartz crystal oscillators, MEMS oscillators produced by Discera Inc. have demonstrated their advantages in smaller size, low power consumption and superior resistance to shocks [13]. These advantages may make their products as potential replacements of the conventional quartz crystal components and become commercially attractive in the coming future.

### 1.3 MOTIVATIONS AND THESIS CONTRIBUTION

The micro-resonator is an elementary structure in the MEMS timing and frequency reference devices. The characteristics of the single resonator play an important role in determining the performance of the applications. From what we can see in Figure 1.5 (a), the free-free beam micromechanical resonator is practically used in the real production of oscillators because of its easy structure as well as the ability to achieve

high performance. However, for the above mentioned free-free beam resonators [8], a special silicon surface micromachining fabrication process is used with a sacrificial oxide thickness of only 130 nm. This process is not available to outside researchers and cannot be massively produced. In addition, the mechanical characterizing performance of the resonator has not been discussed in any of the references. By taking those factors in mind, this thesis will concentrate on the study of flexural mode free-free beam MEMS resonators fabricated by using standard surface micromachining techniques. A mechanic-to-electric analogy is proposed to simulate the electrical characteristics of the resonator as well. Furthermore, the static and dynamic performances in mechanical domain are fully studied by finite element analysis and experimental testing to make the research on MEMS resonators more comprehensive.

In this project, two commercially available fabrication processes, UW-MEMS and PolyMUMPs are used to fabricate the designed free-free beam micro-resonators. Finite element analysis (FEA) is applied for the structural and electro-mechanical simulations. An electrical behavior model is then derived by utilizing direct mechanic-to-electric analogy and simulated by Advance Design System (ADS). The fabricated chips are experimentally tested using Veeco NT-9100 In-Motion System and electrostatic biasing is applied to fine tune the resonators. Electrical testing is carried out as well to obtain the frequency characteristics in electrical domain. Experimental results are analyzed and compared with the theoretical and simulation results.

## **1.4 THESIS OUTLINE**

The thesis is organized as follows:

In Chapter 2, MEMS fabrication techniques are introduced. Free-free beam MEMS resonators are designed and fabricated using two different surface micromachining processes (UW-MEMS and PolyMUMPs). Steps involved in each fabrication process are discussed in detail.

Chapter 3 explains the modeling of the electrostatic actuated free-free beam MEMS resonators. The working principle of the device is described and the parameters of the resonators are carefully selected. Then a direct analogy is proposed from mechanical to electrical domain. The equivalent electrical LCR circuits for the resonators are derived and simulated to predict electrical responses.

Chapter 4 presents the finite element analysis that is carried out to determine the effects of critical structural dimensions and electromechanical coupling. Modal, static and dynamic simulations are shown in this chapter

In Chapter 5, testing and measurement setups are described. The experimental results of the UW-MEMS resonators are compared with analytical solutions and FEA simulation results. Discrepancies are discussed finally.

Chapter 6 summarizes the work of this thesis and suggests the possible future work.

FEA simulation steps and static testing results of PolyMUMPs resonators are provided in the appendices.

## **CHAPTER 2 MEMS FABRICATION PROCESS**

This chapter discusses the fabrication techniques of the MEMS devices. Two main fabrication techniques, bulk and surface micromachining, are described. Two standard surface micromachining processes, UW-MEMS and PolyMUMPS, which are used to fabricate the MEMS resonators in this work, are discussed in detail in this chapter.

### **2.1 MEMS FABRICATION TECHNIQUES**

Many tools and procedures developed for manufacturing MEMS devices are evolved from the IC fabrication process. Similar to the semiconductor industry, fabrication techniques have a decisive effect on performance and reliability of MEMS devices. Micromachining is the foundation of MEMS fabrication, enabling structures and devices with features at the micron scale. Bulk micromachining and surface micromachining are the two basic micromachining techniques used for manufacturing MEMS devices. These techniques can be used to make integrated systems with the functionality that cannot be realized with traditional technologies.

### **2.2 BULK MICROMACHING PROCESS**

Bulk micromachining is a fabrication technique which involves removal of significant amount of materials from a bulk substrate to form a three dimensional geometry of the microstructures, such as membranes, cavities, trench holes, etc (Figure 2.1).

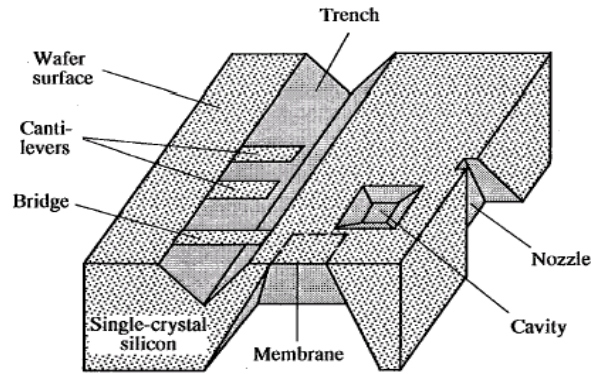


Figure 2. 1: Various bulk micromachining structures [1]

Based on the different types of etchants, bulk micromachining process can be divided into dry etching and wet etching. Plasma or vapor-phase etchants are used for dry etching and liquid chemicals are used for wet etching. A drawback of traditional bulk micromachining is that the geometry of the structures is restricted by the inherent crystallography orientation. Therefore, the resultant devices are always in relatively larger sizes, and it is difficult to make complex structures compared to other micromachining techniques [17]. However, it is less expensive than other micromachining processes and more suitable for simple geometries.

Silicon-on-Insulator (SOI) technology is a typical bulk micromachining process which refers to the use of a layered silicon-insulator-silicon substrate in place of conventional silicon substrates in semiconductor manufacturing, especially in microelectronics. It can reduce parasitic device capacitance due to isolation from bulk silicon, thereby improving power consumption of matched performance. SOI-based devices differ from conventional silicon-built devices in that the silicon junction is above an electrical insulator, typically silicon dioxide or sapphire. The choice of insulator depends largely on the intended application, with sapphire being used for high performance radio frequency and radiation-sensitive applications, and silicon dioxide for diminished short channel effects in microelectronics devices [18]. Additionally, the thickness of the uppermost silicon layer can be determined by using

ion implantation followed by controlled exfoliation method which provides more flexibility for MEMS structures. The first industrial implementation of SOI was announced by IBM in August 1998.

## **2.3 SURFACE MICROMACHINING PROCESS**

Surface micromachining process is the most commonly used technique for fabricating MEMS devices. It evolved directly from IC fabrication methods of patterning, photolithography, deposition, and etching, although there are major differences. A main characteristic of surface micromachining is deposition of multiple materials layer by layer on top of a substrate. The substrate is used as a mechanical support whose properties are not as critical as in bulk micromachining. A mechanical structure is produced by removing sacrificial layer (an oxide layer for example) and releasing structural layer (polysilicon for example). Figure 2.2 shows an example of making a cantilever beam using surface micromachining process [19]. A sacrificial layer is first deposited on top of a substrate and patterned for contacts of the cantilever beam to the substrate. Then a structural layer is deposited onto it, and patterned to form the shape of the cantilever beam. At last, etching of the sacrificial layer releases the final structure.

The dimensions of structures fabricated by surface micromachining techniques can be several orders of magnitude smaller than bulk micromachined structures. Since sacrificial layers have no effects on structural parts and multiple structural, sacrificial layers can be applied, surface micromachining allows fabrication of complex and high resolution micromechanical structures.

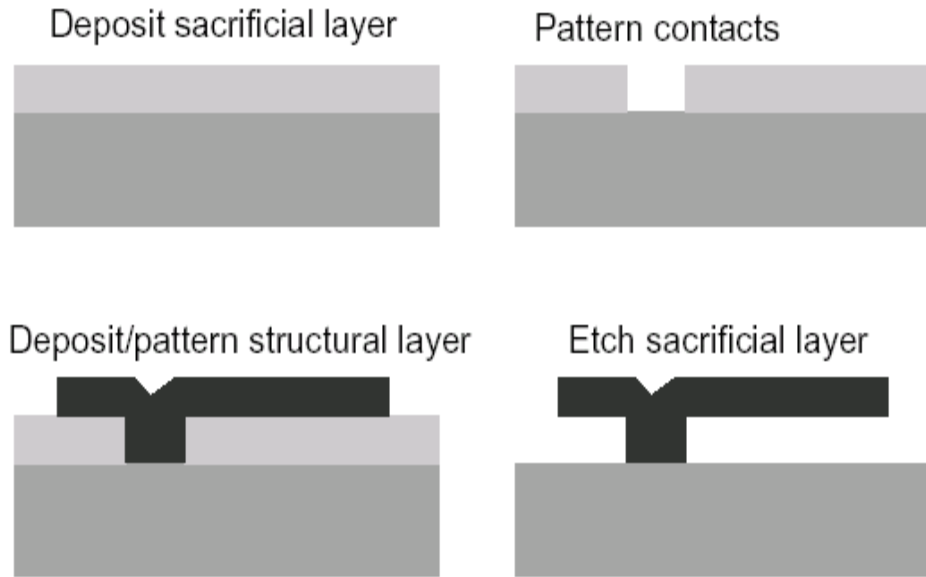


Figure 2. 2: Example of surface micromachining process

The devices described in this thesis are fabricated using two commercially available surface micromachining processes, UW-MEMS process and PolyMUMPs, which will be explained in detail in the following section.

### 2.3.1 UW-MEMS Process

UW-MEMS Process is a cost effective, multi-user MEMS fabrication process developed and offered by the University of Waterloo in Canada in recent years. The process is a gold-based surface micromachining process with seven masks which are optimized for typical RF applications. The process starts with a 0.025” thick Alumina substrate polished on both sides and the real part of the relative permittivity of the substrate is 9.8 with a loss tangent equals to 0.0001 at 1MHz.

Fig. 2.3 to Fig. 2.6 depicts the general fabrication process for a cantilever beam [21]:



Figure 2. 3: Deposition of Chromium and first dielectric layers on the substrate

In Fig. 2.3, after the cleaning of the wafer, the first layer of Cr is deposited and patterned using the lift-off technique. A 0.3  $\mu\text{m}$  of silicon oxide is then deposited and patterned. Reactive Ion Etching (RIE) is employed to pattern the oxide and remove the patterning photo resist.

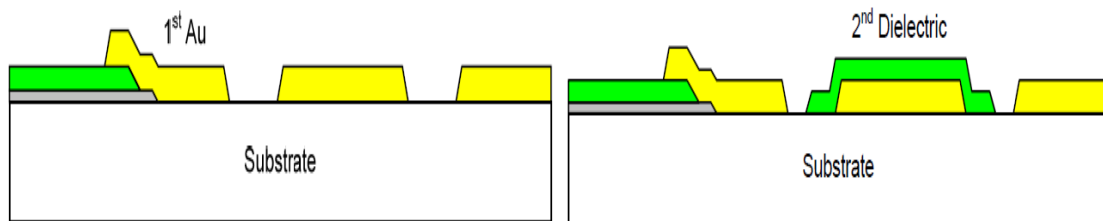


Figure 2. 4: Deposition and patterning of first gold layer and second dielectric layer

In Fig. 2.4 an evaporated 400  $\text{\AA}$  chromium / 100 nm gold bilayer is deposited as a seed layer. A mold is formed in the third lithographic step and 1  $\mu\text{m}$  gold is electroplated inside the mold. A 300  $\text{\AA}$  of Titanium Tungsten (TiW) film as an adhesion is sputtered followed by the deposition of 0.5  $\mu\text{m}$  silicon oxide using plasma enhanced chemical vapor deposition (PECVD). The dielectric and TiW layers are dry etched.

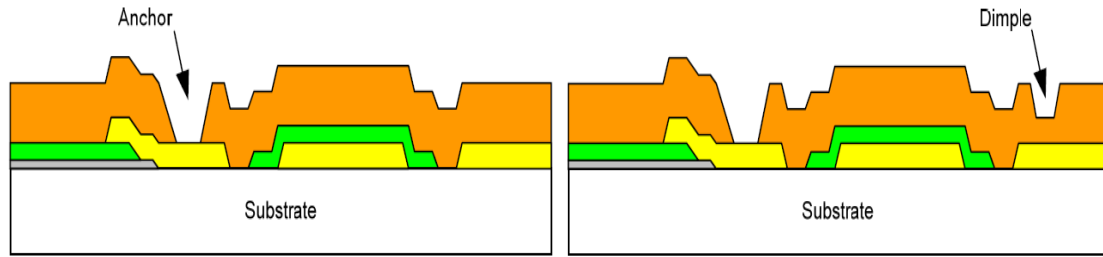


Figure 2. 5: Sacrificial layer deposition and anchor holes, dimple patterning

In Fig. 2.3, spin coated Polyimide is used as the sacrificial layer for this process. Initially, it is coated to a thickness of  $2.5\ \mu\text{m}$ . Next, it is patterned by an anchor mask in an RIE step to etch the Polyimide and fully clear anchor holes. Photo resist mask is used to pattern the dimples in an RIE etching step. The depth of the etching is controlled to be  $1\ \mu\text{m}$ .

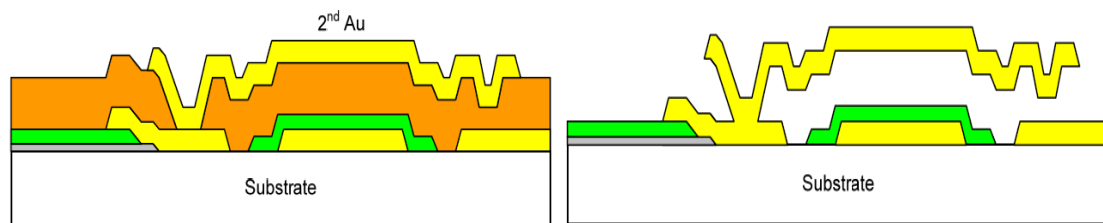


Figure 2. 6: Final structural layer deposition and complete structure after releasing

In Figure 2.6, the top gold layer consists of a gold seed and an electroplated gold layer with the total thickness is  $1.25\ \mu\text{m}$ , and it is used as the structural layer for the devices. The sacrificial layer is removed in an oxygen plasma dry etch process. After releasing, the fabrication steps are complete and prepared for package.

Table 1 outlines the materials, thicknesses and mask levels for each fabrication step of UW-MEMS process. A brief description of each layer with comments is also included [21].

Table 1: Materials, thickness and layer descriptions of UW-MEMS process [21]

Material	Thickness $\mu\text{m}$	Mask Level	Layer Description	Comments
<b>Cr Chromium</b>	0.04	Mask #1	Resistive Voltage Biasing	Resistive Layer
<b>D1 Silicon Oxide</b>	0.3	Masks #2 & #3	Dielectric	Dielectric to cover Cr
<b>G1 Gold 1</b>	1	Mask #4	Conductive Layer	400Å Cr + 1 $\mu\text{m}$ Au
<b>D2 Silicon Oxide</b>	0.5	Mask #5	Dielectric	300Å Cr + 0.5 $\mu\text{m}$ SiO <sub>2</sub>
<b>Sacrificial Layer</b>	2.5	Masks #6 & #7	Sacrificial Layer	2.5 $\mu\text{m}$ Anchor and 1 $\mu\text{m}$ Dimple Openings
<b>G2 Gold 2</b>	1.25	Mask #8 & #9	Top Conductive Layer	0.1 $\mu\text{m}$ Sputtered Au + 1.15 $\mu\text{m}$ Electroplated Au

### 2.3.2 PolyMUMPs

PolyMUMPs, another standard multi-user MEMS process, is a three-layer surface micromachining process derived from the work performed at the Berkeley Sensors and Actuators Center (BSAC) in early 90's [20]. Polysilicon is the structural material of choice due to its fine mechanical properties [16]. The process is different from the most customized surface micromachining processes in that it is designed to be as general as possible, and be capable of supporting many different designs on a single silicon wafer. It provides a cost-effective, proof-of-concept MEMS fabrication for industry and university worldwide. Figure 2.7 shows the PolyMUMPs layers along with their thicknesses.

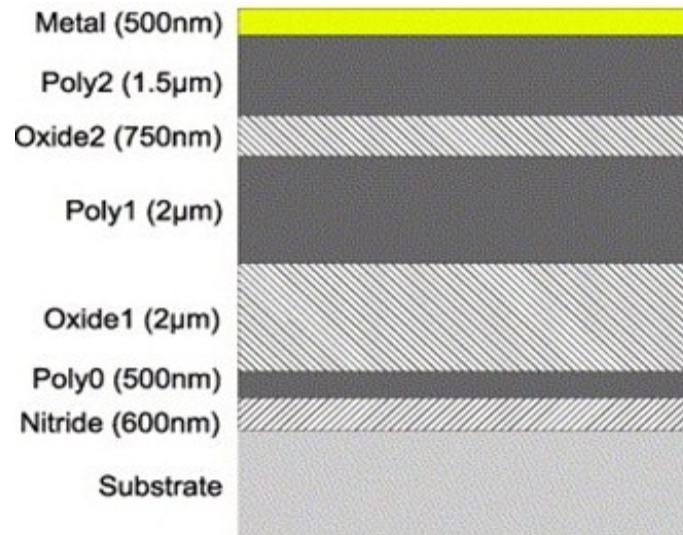


Figure 2. 7: PolyMUMPs layers and their thickness

The process starts from a 1mm thick silicon substrate coated by nitride as an electrical isolation layer. The structural layers are Poly0, Poly1, Poly2 and a metal layer on top for wiring and contact pads. Several modifications and enhancements have been made to increase the flexibility and versatility of the process for the multi-user environment. Since most of the deposition, patterning and etching methods are similar to the UW-MEMS described before, the process flow is not given here. Each layer's function is listed in Table 2.

Table 2: PolyMUMPs layers and their properties [20]

Material Layer	Thickness	Lithography level name	Function
Silicon Nitride	0.6 $\mu m$		Insulator
Poly0	0.5 $\mu m$	Poly0 and Hole0	Conductive Layer
First Oxide	2.0 $\mu m$	Dimple	Release friction
First Oxide	2.0 $\mu m$	Anchor1	Fix poly1 on substrate
Poly1	2.0 $\mu m$	Poly1 and Hole1	Structural layer
Second Oxide	0.75 $\mu m$	Poly1-Poly2-Via	Connect Poly1 and Poly2
Second Oxide	0.75 $\mu m$	Anchor2	Fix POLY2 on substrate
Poly2	1.5 $\mu m$	Poly2 and Hole2	Structrual layer
Metal	0.5 $\mu m$	Metal and Metal Hole	Conductive layer

## 2.4 MEMS RESONATOR LAYOUT

Selection of MEMS sizes has to be appropriate and feasible for fabrication. That means a designer should follow design guidelines and rules which identify physical limitations of individual fabrication process. Otherwise, a MEMS device may not be fabricated correctly. In particular, minimum feature size, referred to the minimum width of a trace that will be feasible with a current fabrication process, should be respected. The same is applied to the minimum gap that specifies the shortest separation distance between two adjacent features. In UW-MEMS, the minimum feature size and gap distance are 10  $\mu\text{m}$  while those of PolyMUMPs are 2  $\mu\text{m}$ . These guidelines and rules are extremely important and needed to be respected at all design stages.

Layout of a device can be drawn using Tanner EDA L-Edit. After design rule check (DRC), a design can be sent to CMC Microsystems for fabrication. Figure 2.8 shows the 3D view of the micro-resonator fabricated with the UW-MEMS process.

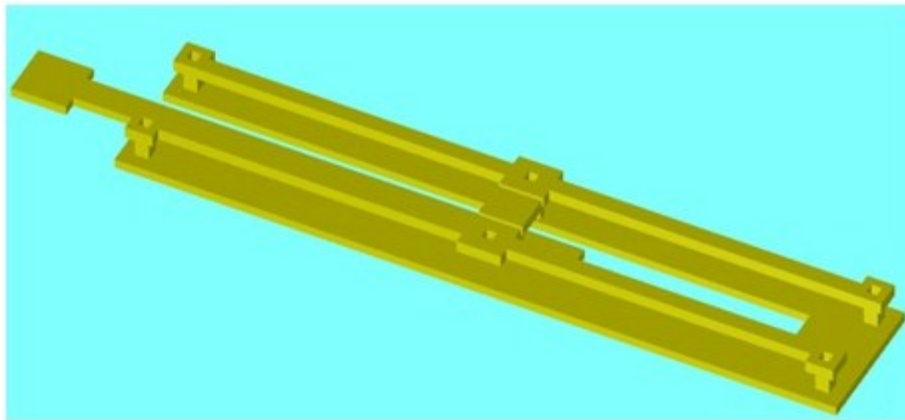


Figure 2. 8: 3D view of UW-MEMS micro-resonator by L-edit

## **2.5 SUMMARY**

A brief introduction of MEMS fabrication techniques is provided in this chapter. Two standard surface micromachining processes suitable for micro-resonator design are described in detail. Layouts using both of the UW-MEMS process and PolyMUMPs are shown as well.

## CHAPTER 3 THE FREE-FREE BEAM MEMS RESONATOR

This chapter introduces the design, working principle and modeling of the free-free beam micromechanical resonator.

### 3.1 RESONATOR STRUCTURE AND OPERATION

Figure 3.1 shows the structure of the free-free beam resonator along with appropriate bias, excitation and off-chip readout circuitry. Figure 3.2 presents the top view of the structure. As shown, the resonator consists of a vibrating beam, mechanically supported at its nodal points by four torsional supporting beams [10]. Each of the supporting beams is suspended above the ground plane and rigidly anchored to the substrate at the end. A conductive electrode is provided beneath the vibrating beam, serving as the capacitive driving electrode to allow electrostatic actuation in the vertical (perpendicular to the substrate) direction.

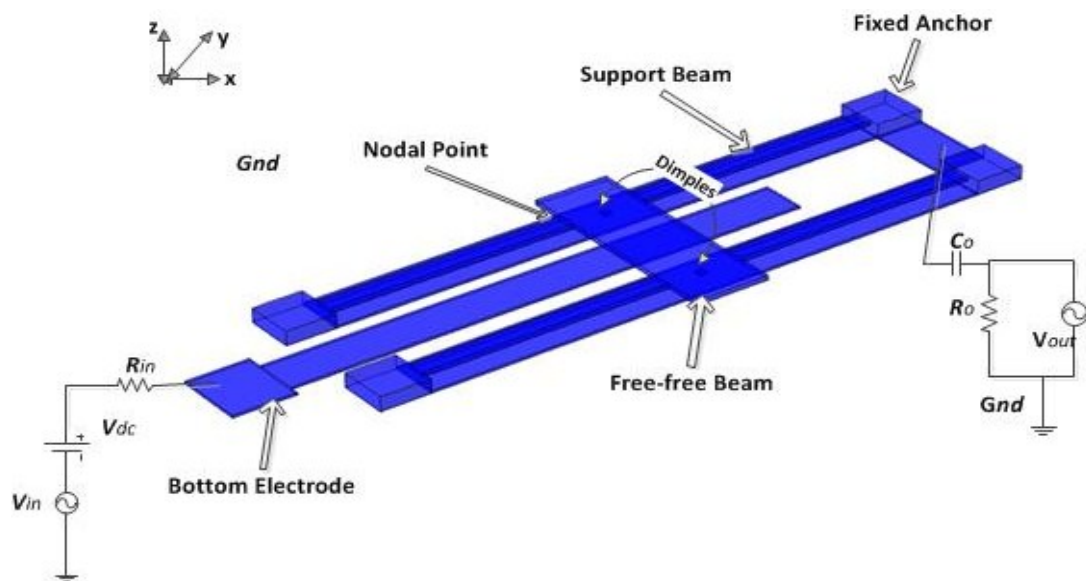


Figure 3. 1: 3D view of the free-free beam resonator

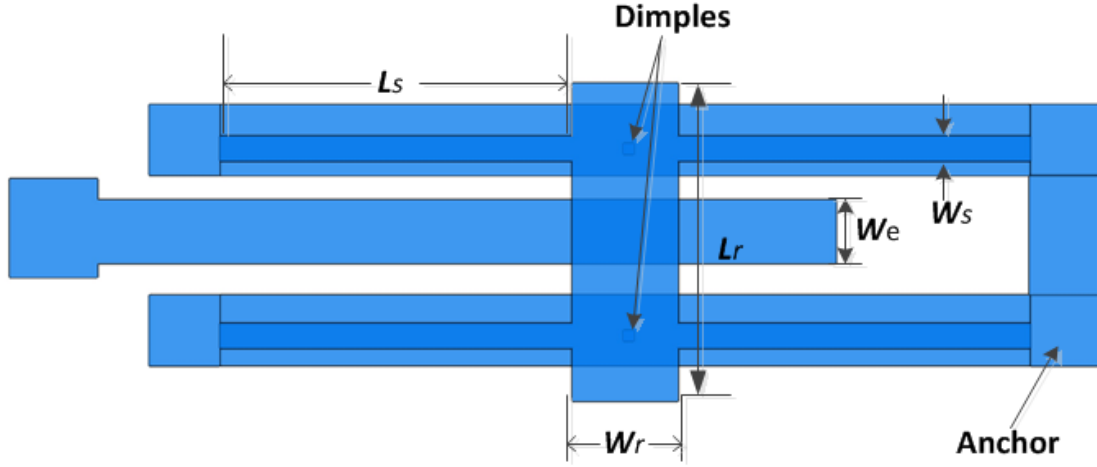


Figure 3. 2: Top view of the resonator structure

To enable the device, an electrostatic force is created by applying a DC bias voltage  $V_{dc}$  between the bottom electrode and the resonator structure. An AC input excitation induces the resonator vibration at the frequency of  $(V_{ac})_{in}$ , and the detected output current  $i_{out}$  is generated by the action of time-varying resonator-to-electrode capacitor given by:

$$i_{out} = V_{dc} \frac{\partial C}{\partial t} = V_{dc} \frac{\partial C}{\partial z} \frac{\partial z}{\partial t} \quad (3.1)$$

where  $z$  is the vertical displacement and  $\partial C / \partial z$  is the change of capacitance per unit displacement between electrode and vibrating beam [14].

When the frequency of the applied  $V_{in}$  reaches the natural frequency of the resonator, the beam starts to vibrate at the maximum amplitude so that  $\partial z / \partial t$  has the greatest value. In this thesis, the resonator is intended to vibrate in its fundamental mode, so the frequency of the input voltage should be tuned in an appropriate range, avoiding excitation of second or higher mode of vibration. To allow sensing of the output current  $i_{out}$  from the resonator structure while also applying the dc bias  $V_{dc}$ , an off-chip readout circuit consisting of the capacitor is utilized as shown in Figure 3.1.

As shown in Figure 3.3, when a sufficiently large  $V_{dc}$  is applied between the electrode and resonator, the entire structure is pulled down and sits upon the dimples, which are located at flexural nodal points. As a result, the transducer capacitor gap is no longer exclusively determined by the sacrificial layer, of which the thickness is  $g_{ini}$ . Rather, the gap spacing in operation is now dependent on the height of the dimples, given by  $g_0$ , which is set via a timed etch in the UW-MEMS process.

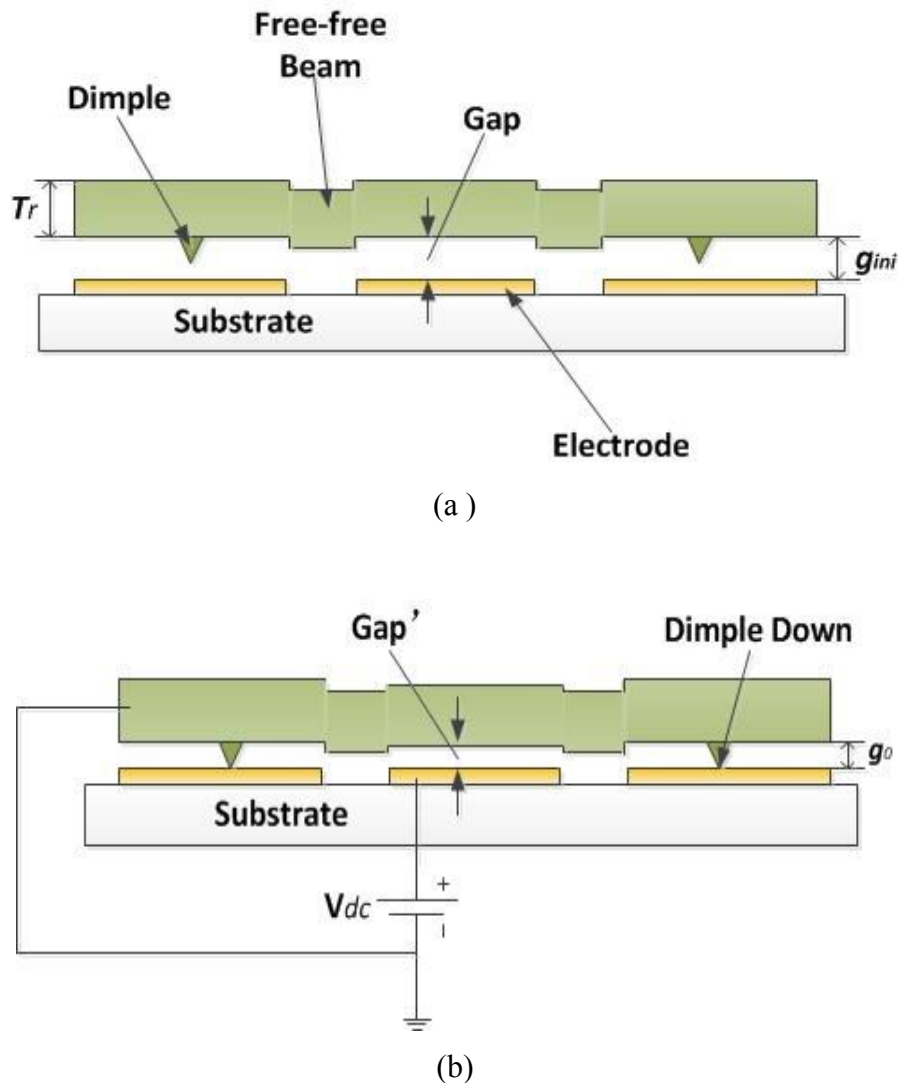


Figure 3. 3: (a) Cross section view of a structure after fabrication and before operation, (b) After application of a large enough DC voltage to attract dimples down.

There are three advantages of using dimples to set the capacitor gap: 1) No catastrophic pulling-down of the resonator when bias voltage is applied, 2) Much

higher device quality factor compared to the clamp-clamp beam resonator, 3) Lower DC voltage than that with other MEMS resonators because the final gap spacing is determined by the height of the dimples, regardless the thickness of the sacrificial layer [10].

## 3.2 MATHEMATICAL MODEL

### 3.2.1 Resonant Frequency Design

The simplest case of a mechanical resonance system consists of a mass  $m$  attached to a spring  $k$  and the resonance frequency is governed by the general expression [25]:

$$f = \frac{1}{2\pi} \sqrt{\frac{K}{M}} \quad (3.2)$$

For a cantilever beam under various boundary and loading conditions, its vibration mode is described by Euler-Bernoulli beam theory and the resonant frequency of a uniform beam with even load can be derived from the above equation and result in [26]:

$$f_n = \frac{(\beta_n l)^2}{2\pi} \sqrt{\frac{EIg}{wL_r^4}} = \frac{(\beta_n l)^2}{4\pi\sqrt{2}} \sqrt{\frac{E}{\rho} \frac{T_r}{L_r^2}} \quad (3.3)$$

where  $E$  and  $\rho$  are the Young's modulus and the density of material, respectively.  $L_r$  and  $T_r$  are length and thickness of the beam which are specified in Figure 3.2. Moment of inertia  $I$  for the case of large  $L_r$ -to- $T_r$  ratio is  $W_r T_r^3/12$ ,  $w$  is distributed

force per unit length,  $\beta_n l$  for  $n=1$  to  $\infty$  is the characteristic for the vibration mode shape function which is given in the general form:

$$W_{(y)} = A \sin \beta_n y + B \cos \beta_n y + C \sinh \beta_n y + D \cosh \beta_n y \quad (3.4)$$

The values for  $\beta_n$  and four constants of integration  $A$ ,  $B$ ,  $C$ , and  $D$  will be determined by the end constraint and loading conditions [27]. Modal analysis is the key to finding an accurate lumped model that includes the effects of material and force distribution and modal behavior of the system. Table 3 lists the normalized mode shape for the beams in common boundary conditions.

Table 3: Mode shape for a vibration beam in various boundary conditions [28]

Boundary Condition	Characteristic Equation	$\beta_n l$	Normal Mode Shapes $W_n(x)$	$\sigma_n$
Free-Free	$\cos \beta l \cosh \beta l = 1$	0 (Rigid Body)	$\cosh \beta_n x + \cos \beta_n x$ $-\sigma_n (\sinh \beta_n x + \sin \beta_n x)$	0.9825
		4.73004074		1.0008
		7.85320462		0.9999
		10.99560780		1.0000
		14.1371655		0.9999
		17.2787597		1, $n > 5$
	$\frac{(2n+1)\pi}{2}, n > 5$			
Clamped-Free	$\cos \beta l \cosh \beta l = -1$	1.87510407	$\cosh \beta_n x - \cos \beta_n x$ $-\sigma_n (\sinh \beta_n x - \sin \beta_n x)$	0.7341
		4.69409113		1.0185
		7.85475744		0.9992
		10.99554073		1.0000
		14.13716839		1.0000
		17.2787597		1, $n > 5$
	$\frac{(2n-1)\pi}{2}, n > 5$			
Clamped-Clamped	$\cos \beta l \cosh \beta l = 1$	4.73004074	$\cosh \beta_n x - \cos \beta_n x$ $-\sigma_n (\sinh \beta_n x - \sin \beta_n x)$	0.9825
		7.85320462		1.0008
		10.9956079		0.9999
		14.1371655		1.0000
		17.2787597		0.9999
		17.2787597		1, $n > 5$
	$\frac{(2n+1)\pi}{2}, n > 5$			

By substituting the values of the above table in equation (3.3) and (3.4), the fundamental mode frequency of a free-free beam in the vertical direction is:

$$f_0 = 1.03 \sqrt{\frac{E T_r}{\rho L_r^2}} \quad (3.5)$$

And the mode shape function  $W_{(y)}$  is:

$$W_{(y)} = \cosh \frac{4.73}{L_r} y + \cos \frac{4.73}{L_r} y - 0.9825 \left( \sin \frac{4.73}{L_r} y + \sinh \frac{4.73}{L_r} y \right) \quad (3.6)$$

where  $y$  is a point along the beam length and  $W_{(y)}$  is the deflection of the beam at that point.

As it can be seen from the equation 3.5, the resonant frequency of the beam depends on the length and thickness of the beam if the structural material is fixed. The resonator beam width  $W_r$  is governed by length-to-width ratio design consideration for the most practical design. While the thickness  $T_r$  is determined primarily by processing constraints, the length of the beam  $L_r$  becomes the principal variable to determine the resonance frequency. This can be plotted in a contour plot as shown in Figure 3.4, which defines the center frequency of the resonator with respect to  $L_r$ , using both UW-MEMS process and PolyMUMPs. The thickness  $T_r$  of the structural layer, Young's modulus and the density of the materials for each process are indicated in the plot as well.

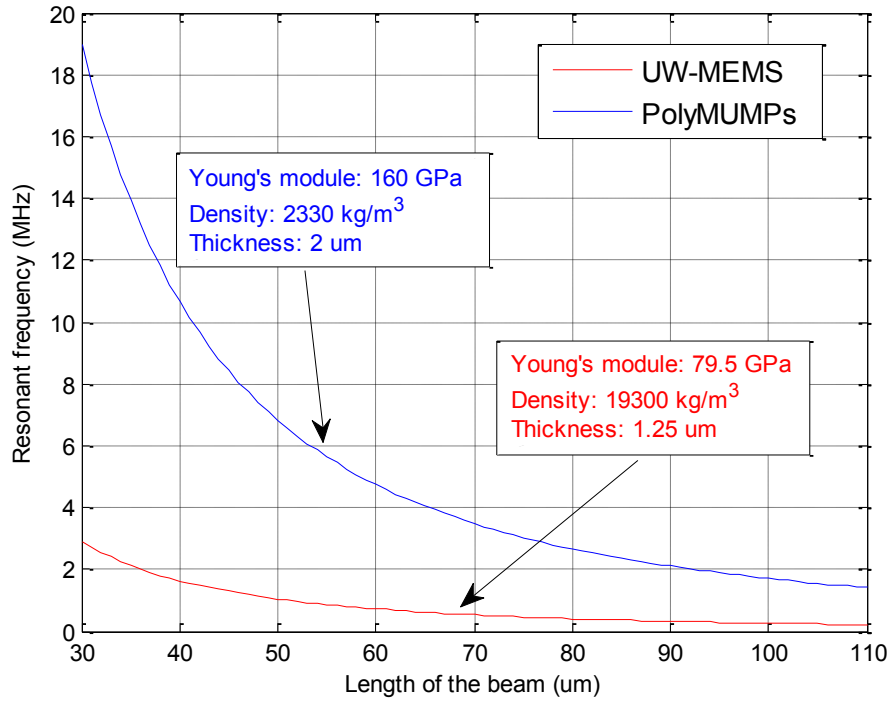


Figure 3. 4: Plot for resonant frequency against beam length for two processes

These curves help to set the beam dimensions for desired frequencies, considering all the fabrication limits. As we can easily find out from the plot, devices fabricated with PolyMUMPs can have much higher operation frequencies than those of UW-MEMS process.

### 3.2.2 Support Structure Design

In clamped-clamped beam resonators, both ends of resonant beams are fixed to a substrate by anchors, which result in energy loss [7]. The free-free beam resonator is to suppress anchor power dissipation, allowing much higher device quality factor (Q). To retain the basic flexural-mode beam, torsional supporting beams are strategically designed with quarter-wavelength dimensions so that anchors and their associated losses are ideally eliminated.

As identified in Figure 3.1, the free-free beam resonator is supported at its fundamental-mode nodal points by four torsional beams. The exact positions of nodal points for a single beam can be evaluated by setting the normalized mode shape function  $W(y)$  (equation 3.4) to zero and solving for  $y$ . Take a 100  $\mu\text{m}$  beam for an example, its vibrating nodal points are located at the positions of 22.41  $\mu\text{m}$  and 77.59  $\mu\text{m}$ , presented in Figure 3.5.

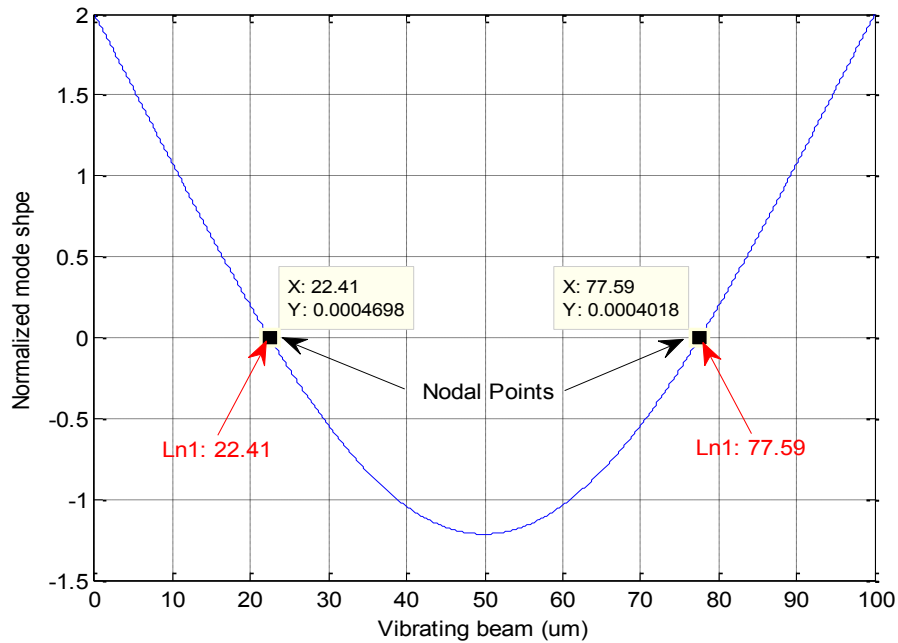


Figure 3. 5: Plot of the normalized fundamental mode shape for a 100  $\mu\text{m}$  beam

Since attached at the nodal points, the supporting beams ideally sustain no translational movement during resonator vibration. Furthermore, since the characteristics of a small cross section beam are similar to the characteristics of an electrical transmission line, torsional losses (caused by torsional strain of the supporting beams during vibration) can also be suppressed by choosing appropriate support dimensions [29]. In particular, the length of a torsional supporting beam is designed as a quarter-wavelength so that an impedance transformation isolates the free-free beam from the rigid anchors. Ideally, the solid anchor condition on one side of the support beam is transformed to a free end condition on the other side, which connects to the resonator. In terms of impedance, the infinite impedance at the

anchors is transformed to zero impedance at the resonator attachment points. As a result, the free-free beam resonator effectively operates as if levitated without associated losses and need of supports.

The above transformation for torsional beams analysis can be found in the literature [5]. In general, a **T** network is commonly modeled for the torsional beam as shown in Figure 3.6.

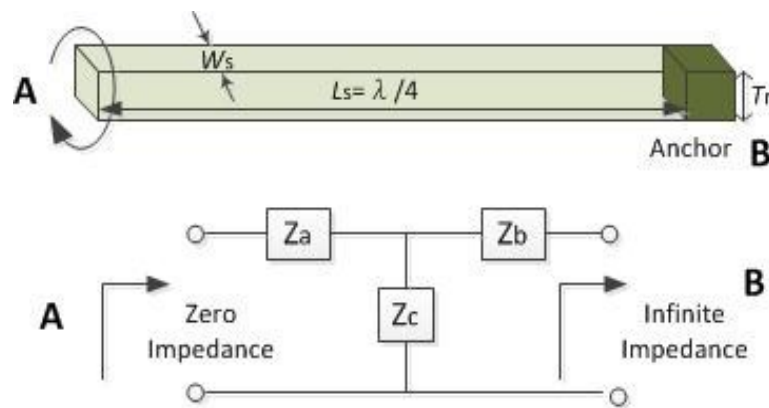


Figure 3. 6: Quarter-wavelength torsional beam with B side anchoring and equivalent acoustic network showing zero impedance at port A with port B open

The shunt and series arm impedances of the network can be derived through appropriate **T** network analysis [25]. When the length of a given support beam corresponds to the effective quarter-wavelength of the operating frequency, the relationship between the effective impedance  $Z_a$ ,  $Z_b$  and  $Z_c$  are obtained as:

$$Z_a = Z_b = -Z_c \quad (3.7)$$

Given that the impedance of the anchor at side B is infinite, it is clear that due to cancellation of the remaining impedance in the network, the impedance seen at port A is zero.

Since the thickness of the torsional support beam  $T_r$  is usually fixed due to the fabrication process limitations, the length of the beam  $L_s$  of the effective quarter-wavelength beam should satisfy the expression [10]:

$$L_s = \frac{1}{4f_0} \sqrt{\frac{G\gamma}{\rho J_s}} \quad (3.8)$$

where  $J_s$  is the polar moment of inertia,  $G$  is the shear Young's modulus and  $\gamma$  is the torsion constant given by:

$$J_s = T_r W_s \frac{(T_r^2 + W_s^2)}{12} \quad (3.9)$$

$$G = \frac{E}{2(1 + \nu)} \quad (3.10)$$

$$\gamma = \alpha W_s T_r^3 \quad (3.11)$$

Here, the width of the beam  $W_s$  is best chosen as small as possible to reduce the polar moment of inertia, which makes supporting beams easier to rotate,  $\nu$  is the Poisson ratio of the material, and the value of the coefficient  $\alpha$  is determined by the ratio of  $T_r$  to  $W_s$ , as listed in Table 4.

Table 4: The torsion constant coefficient with different side ratios [26]

$W_s/T_r$	1	1.5	2	3	4	5	6	8	10	infinite
$\alpha$	0.141	0.196	0.229	0.263	0.281	0.291	0.299	0.305	0.312	0.333

It should be noted that the stiffness of the support beam  $K_s$ , given by the fixed-free cantilever beam analysis, is:

$$K_s = \frac{E W_s T_r^3}{4 L_s^3} \quad (3.12)$$

### 3.2.3 Electromechanical Coupling

As discussed in the structure and operation section, the transducer capacitor is formed between the resonator beam and the underneath electrode. By applying an appropriate DC bias potential  $V_{dc}$  and an AC signal  $V_{in}$ , an electrostatic force is generated between the transducer capacitor to actuate the resonator, the most dominant component at the frequency of  $V_{in}$  is then given by:

$$F = V_{dc} \frac{\partial C}{\partial z} V_{in} \quad (3.13)$$

where  $\partial C / \partial z$  is the change in the electrode-to-resonator capacitance per unit displacement of the resonator, approximately given by (neglecting the beam bending and fringing effect):

$$\frac{\partial C}{\partial z} \approx \frac{\epsilon_0 W_r W_e}{g_0^2} \quad (3.14)$$

Here,  $g_0$  is the gap spacing between electrode and resonator under DC bias conditions as shown in Figure 3.3 (b).  $W_s$  and  $W_e$  are defined as shown in Figure 3.2.

For the practical design, it is often necessary to define an equivalent mechanical model with mass, spring and damper, as shown in Figure 3.7 for this resonator.

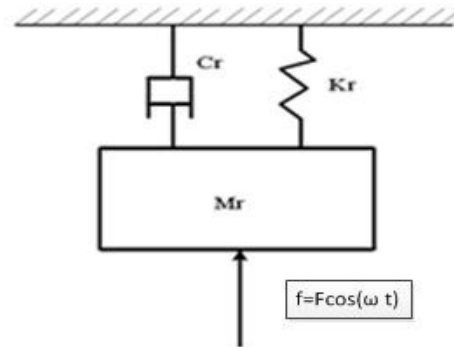


Figure 3.7: A simple mechanical system with mass, spring and damper

Using the mode shape function of the system, the equivalent lumped parameters for the beam, such as mass  $M_r$ , stiffness  $K_r$  and damping factor  $C_r$  are given by [30]:

$$M_r = \rho W_r T_r \int_0^{L_r} W_{(y')}^2 dy' \quad (3.15)$$

$$K_r = \omega_0^2 M_r = (2\pi f_0)^2 M_r \quad (3.16)$$

$$c_r = \frac{\sqrt{M_r K_r}}{Q_0} \quad (3.17)$$

where  $\omega_0$  is the radian resonance frequency and  $Q_0$  is the quality factor of the resonator.

Sometimes, we are interested in equivalent lumped parameters at a specific location along the beam (such as center point or nodal points). In such a case, the distributed parameters have to be developed. Since the total kinetic energy of the distributed system is to be equal to the lumped model [31], the parameters with element values that vary with locations on the resonator can be written as:

$$M_{(y)} = \frac{2K_{E_{total}}}{V_{(y)}^2} = \frac{\rho W_r T_r \int_0^{L_r} W_{(y')}^2 dy'}{W_{(y)}} \quad (3.18)$$

$$K_{(y)} = \omega_0^2 M_{(y)} = (2\pi f_0)^2 M_{(y)} \quad (3.19)$$

$$c_{(y)} = \frac{\sqrt{M_{(y)} K_{(y)}}}{Q_0} \quad (3.20)$$

Here,  $K_{E_{total}}$  is the peak kinetic energy of the resonator,  $V_{(y)}$  is the velocity at location  $y$  along the beam length.  $M_{(y)}$ ,  $K_{(y)}$  and  $c_{(y)}$  are the equivalent mass, spring stiffness and damping factor of the beam at location  $y$  along the beam length. Dimensional

parameters are given in Figure 3.8. The velocity at any point is the partial differentiation of the normalized mode shape  $W(y)$  with respect to time.  $W(y)$  for beams is given by equation (3.6).

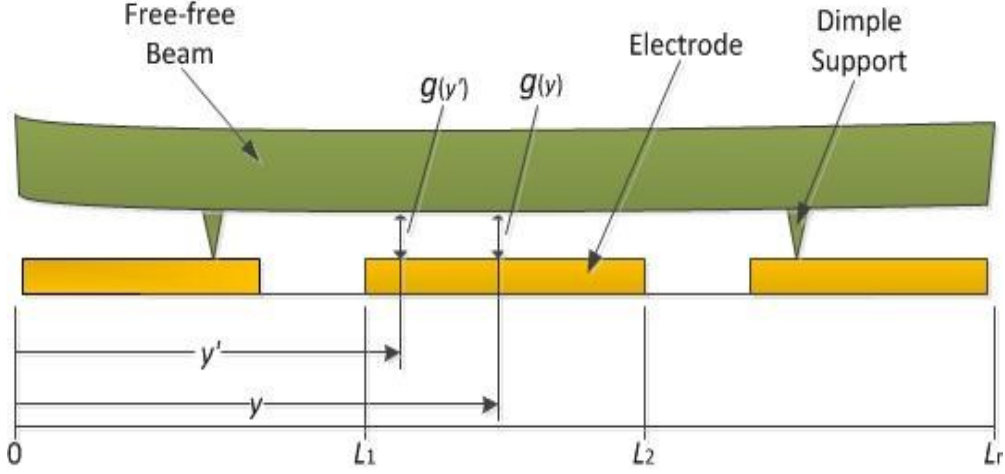


Figure 3. 8: Cross section schematic of a free-free beam resonator, indicating key variables used in formulations

Because the electrode-to-resonator capacitance is a nonlinear function of beam displacement, the capacitive electromechanical coupling should be taken into consideration when calculating the resonance frequency of the device. In fact, the  $V_{dc}$ -dependent electrostatic force from equation (3.13) will lead to a softening effect on the total stiffness of the beam. This effect can be modeled by an electrical spring constant  $K_e$ , which combines with the mechanical stiffness of the beam  $K$ , making the total spring stiffness  $K_r=K-K_e$ . The effective resonance frequency of the resonator is lower than its natural frequency due to a decrease of the effective stiffness [9]:

$$f = \frac{1}{2\pi} \sqrt{\frac{K_r}{M}} = f_0 \sqrt{1 - \frac{K_e}{K}} = 1.03 \sqrt{\frac{E}{\rho} \frac{T_r}{L_r^2}} \left( \sqrt{1 - \frac{K_e}{K}} \right) \quad (3.21)$$

The electrical spring stiffness  $K_e$  is generated by the nonlinear gap capacitance and is strongly dependent upon the electrode-to-resonator gap spacing  $g(y)$ . At a specific

location  $y'$  centered on an infinitely small width of the electrode  $dy'$ , the differential in electrical stiffness is given by:

$$dK_{e(y')} = V_{dc}^2 \frac{\varepsilon_0 W_r dy'}{[g(y')]^3} \quad (3.22)$$

where the gap spacing  $g(y)$  is the difference between the initial gap and the deflection at each location  $y'$  along the beam length due to applied voltage at that point. Thus the gap space at stable equilibrium position can be expressed as:

$$g(y) = g_0 - \int_{L_1}^{L_2} \frac{\varepsilon_0 W_r V_{dc}^2}{2K_{(y')} [g(y')]^2} \frac{W(y)}{W(y')} dy' \quad (3.23)$$

where  $g_0$  is the capacitor gap determined by height of dimples and the second term is the static displacement of the beam at a particular location while applying a set value  $V_{dc}$ , evaluated by integration over the width of the electrode. Since the desired variable  $g(y)$  appears on both side of the equation, equation (3.23) is best solved by assuming  $g(y)=g_0$  at first on the right side, solving for  $g(y)$  on the left and then using the new value to iterate until  $g(y)$  converges within a reasonable tolerance [32]. In this thesis, the electrode is placed under the resonator beam center; thus  $L_1 = 0.5(L_r - W_e)$  and  $L_2 = 0.5(L_r + W_e)$ . The maximum displacement occurs at the center of the resonator beam, where  $y = L_r/2$ .

Combining equation (3.22) and (3.23), the quantity  $\frac{K_e}{K}$  can now be found by integrating over the electrode width from  $L_1$  to  $L_2$ :

$$\frac{K_e}{K} = \int_{L_1}^{L_2} \frac{dK_{e(y)}}{K(y)} = \int_{L_1}^{L_2} \frac{\varepsilon_0 W_r V_{dc}^2}{K(y) [g(y)]^3} dy \quad (3.24)$$

Therefore, the final expression for the resonance frequency of a free-free beam resonator can be modified as follows:

$$f = 1.03 \sqrt{\frac{E}{\rho} \frac{T_r}{L_r^2}} \left( \sqrt{1 - \int_{L_1}^{L_2} \frac{\epsilon_0 W_r V_{dc}^2}{K_{(y)} [g_{(y)}]^3} dy} \right) \quad (3.25)$$

As seen in equation 3.25, the resonance frequency of resonator is a function of DC-bias voltage  $V_{dc}$ , and this can be used advantageously to tune the center frequency of the device. The relationship between applied voltage and the center frequency for a designed resonator is presented later in Figure 4.6.

### 3.2.4 Control Voltage

The applied DC-bias voltage  $V_{dc}$  will not only generate an electrostatic force between the beam and electrode to actuate the device, but will also have a major effect on the frequency characteristic of the resonator due to electromechanical coupling. With this in mind, the value of  $V_{dc}$  should be chosen wisely. Under a normal operation, the free-free beam resonator must be pulled down onto its supporting dimples at nodal points. For most applications, only when the dimples are “down” is the electrode-to-resonator gap spacing small enough to provide adequate electromechanical coupling. On the other hand, with increasing voltage, there will be a specific position at which the stability of the equilibrium is lost and the beam collapses toward the substrate. This is called the pull-in phenomenon. Therefore, the designed voltage should be designed sufficiently large to pull the resonator down onto its dimples, but small enough to avoid the catastrophic pull-in phenomenon.

Symbolically,  $V_{dc}$  must satisfy the relation

$$V_{pull\_in} > V_{dc} > V_{dimple}$$

Since the supporting beams are often much more compliant than the free-free resonator beam (generally, the effective stiffness at the midpoint of the free-free resonator beam is more than 100 times larger than the combined stiffness of the supporting beams), very little bending occurs in the resonator itself when pulling the dimples down. Thus, the restoring force is mostly yielded by supporting beams alone and uniformly over the electrode. Then the expression of the dimple-down voltage  $V_{dimple}$  can be obtained through parallel plate capacitor stability analysis in [2] as

$$V_{dimple} = \sqrt{\frac{8}{27} \frac{K_{com} g_{ini}^3}{W_r W_e}} \quad (3.26)$$

where  $K_{com}$  is the combined stiffness of all the supporting beams, which is four times of  $K_s$  in equation (3.12), and  $g_{ini}$  is the initial electrode-to-resonator gap before the beam is brought down to its dimples.

Once the dimples are down, further movement of the resonator beam towards the electrode is attained via bending of the resonator itself. Then the resonator is considered as a distributed system and the electromechanical coupling analysis in section 3.2.3 is applicable for predicting the catastrophic pull-in voltage  $V_{pull-in}$ . The procedure for evaluating  $V_{pull-in}$  is to set equation (3.24) to unity and then solve for the variable  $V_{dc}$ . The relationship between the bias voltage and the value of  $\frac{K_e}{K}$  for a 100  $\mu\text{m}$  UW-MEMS resonator using the parameters in Table 5 is plotted in Figure 3.9.

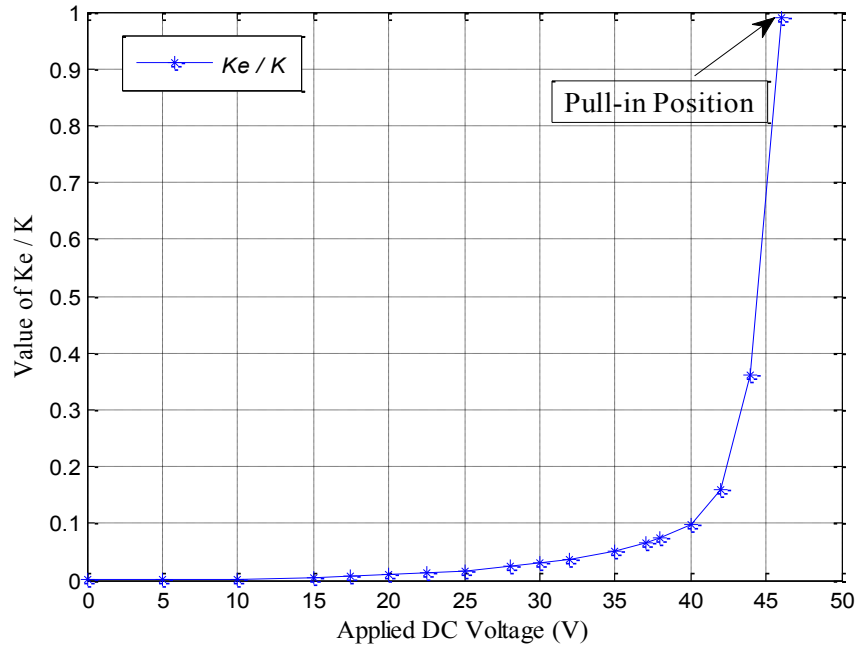


Figure 3. 9: Value of  $K_e / K$  against the applied DC voltage bias

As shown, the stiffness soften effect of the system is more evident as the bias voltage increases beyond 30 volts. With dimple-down and pull-in phenomena in mind,  $V_{dc}$  is better to be chosen around 25 V to make sure the resonator can be actuated and operate normally and safely.

### 3.3 MICRO-RESONATOR DESIGN PARAMETERS

From the above description, we know that a variety of parameters need to be taken into consideration to make the device operate well. By considering the above mentioned factors, a 100  $\mu\text{m}$  free-free beam micro-resonators with frequency of 263.6 kHz was designed and fabricated using the UW-MEMS process. For the purpose of performance comparison, a 49.4  $\mu\text{m}$  resonator retaining a similar structure was fabricated by utilizing the PolyMUMPs with frequency targeting at 7 MHz. Table 5

and Table 6 summarize the design parameters and analytical values for the free-free beam resonators, respectively.

Table 5: Free-free beam resonator design parameters in the UW-MEMS process

No.	Parameter	Source	Target	Unit
			Frequency	
			263.6 kHz	
1	Beam Length, $L_r$	Designed	100	$\mu\text{m}$
2	Beam Width, $W_r$	Designed	35	$\mu\text{m}$
3	Beam Thickness, $T_r$	Process	1.25	$\mu\text{m}$
4	Nodal Point 1, $L_{n1}$	Equation (3.6)	22.4	$\mu\text{m}$
5	Nodal Point 2, $L_{n2}$	Equation (3.6)	77.6	$\mu\text{m}$
6	Support Beam Length, $L_s$	Equation (3.9)	255	$\mu\text{m}$
7	Support Beam Width, $W_s$	Designed	10	$\mu\text{m}$
8	Electrode Width, $W_e$	Designed	26	$\mu\text{m}$
9	Initial Gap, $g_{ini}$	Process	2.5	$\mu\text{m}$
10	Dimple Height, $g_0$	Process	1	$\mu\text{m}$
11	Dimple-down Voltage, $V_d$	Equation (3.26)	18.8	V
12	Pull-in Voltage, $V_{pull-in}$	Equation (3.24)	45.9	V
13	DC bias Voltage, $V_{dc}$	Designed	25	V
14	Displacement ( $y = L_r/2$ )	Equation (3.23)	0.021	$\mu\text{m}$
15	Torsion Coefficient, $\alpha$	Table 4	0.305	–
16	Poisson Ratio, $\nu$	Material property	0.43	–

Table 6: Free-free beam resonator design parameters in PolyMUMPs

No.	Parameter	Source	Target Frequency	Unit
			7 MHz	
1	Beam Length, $L_r$	Designed	49.4	$\mu\text{m}$
2	Beam Width, $W_r$	Designed	18	$\mu\text{m}$
3	Beam Thickness, $T_r$	Process limitation	2	$\mu\text{m}$
4	Nodal Point 1, $L_{n1}$	Equation (3.6)	11.1	$\mu\text{m}$
5	Nodal Point 2, $L_{n2}$	Equation (3.6)	38.3	$\mu\text{m}$
6	Support Beam Length, $L_s$	Equation (3.9)	126	$\mu\text{m}$
7	Support Beam Width, $W_s$	Designed	3	$\mu\text{m}$
8	Electrode Width, $W_e$	Designed	13.2	$\mu\text{m}$
9	Initial Gap, $g_{ini}$	Process limitation	2	$\mu\text{m}$
10	Dimple Height, $g_0$	Process limitation	0.75	$\mu\text{m}$
11	Dimple-down Voltage, $V_d$	Equation (3.26)	22.5	V
12	Pull-in Voltage, $V_c$	Equation (3.24)	137	V
13	DC bias Voltage, $V_{dc}$	Designed	40	V
14	Displacement ( $y = L_r/2$ )	Equation (3.23)	0.039	$\mu\text{m}$
15	Torsion Coefficient, $\alpha$	Table 4	0.196	–
16	Poisson Ratio, $\nu$	Material property	0.226	–

It should be noted that PolyMUMPS micro-resonators are approximately two times smaller than the UW-MEMS ones because of fewer fabrication limitations so that a much higher center frequency can be obtained.

Photographs of the fabricated resonators are taken by a Veeco NT-9100 optical profiler. Figure 3.10 shows the picture of a 100  $\mu\text{m}$  free-free beam resonator.

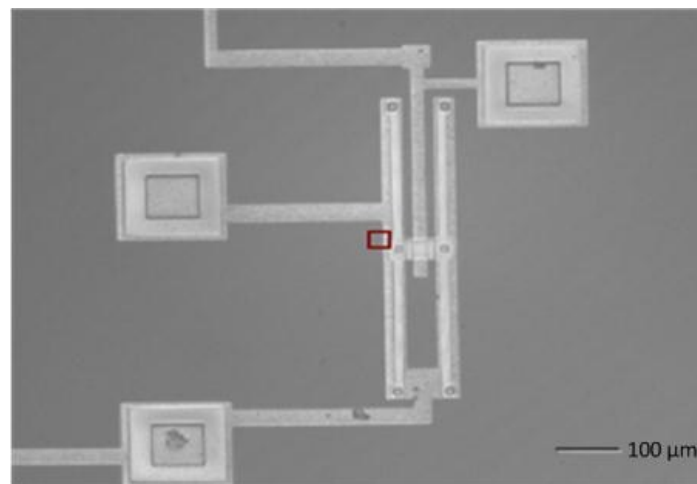


Figure 3. 10: Photograph of a fabricated 100  $\mu\text{m}$  free-free beam resonator

### **3.4 SMALL-SIGNAL ELECTRICAL EQUIVALENT CIRCUIT**

#### **3.4.1 Mechanic to Electric Analogy**

As discussed in Chapter 1, a MEMS resonator can be used as a core part of band-pass filters or oscillators. Consequently, its electrical characteristics are critical. In terms of energy exchange, the applied electrical input signal is first transformed to mechanical energy to induce movement of the resonator, and then transformed back to the electrical output through the capacitive transducer [33]. Such a transformation is

shown in Figure 3.11. Since the behavior of the resonator in the mechanical domain, like displacement and vibration, cannot be analyzed and presented in a straightforward manner with an electrical method. To resolve the issue, an equivalent electrical circuit model can be developed to simulate the electrical characteristics as describe below.

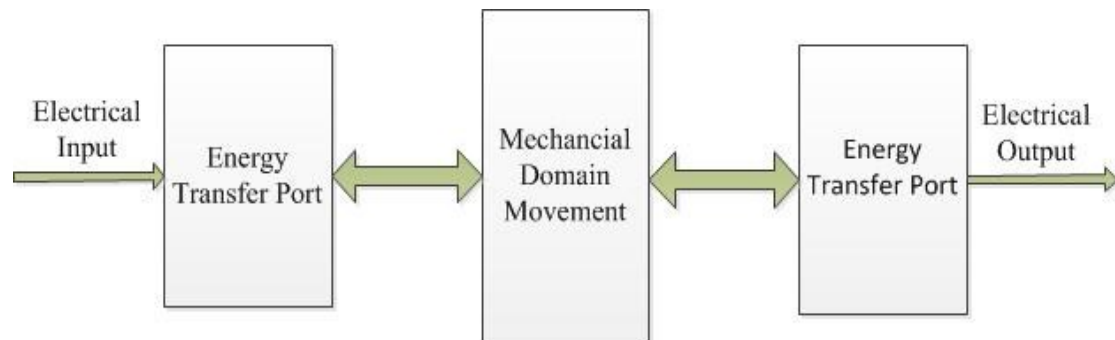


Figure 3. 11: Signal and energy transformation flow graph

Earlier in this chapter, a mechanical system with mass, spring and damper was already defined for the resonator. Electrical circuits can then be modeled based on the direct analogy that exists between electrical and mechanical phenomena. More specifically, let's comparing the following two equations:

$$F = m \frac{\partial v}{\partial t} = m \frac{\partial^2 x}{\partial t^2} \quad (3.27)$$

$$V = L \frac{\partial i}{\partial t} = m \frac{\partial^2 q}{\partial t^2} \quad (3.28)$$

As seen, the force  $F$  plays the same role as the voltage  $V$ , the velocity  $v$  as the current  $i$ , and the displacement  $x$  as the charge  $q$ . The force is analogous to the voltage based on the similarity between two phenomena.

For a simple mechanical vibration system consists of a mass  $M_r$ , a spring  $K_r$  and a damper  $C_r$  under an external force  $f = F\cos\omega t$  shown in Figure 4.1, the system equation can be written in Fourier form as:

$$F = j\omega M_r X + \frac{K_r}{j\omega} X + c_r X \quad (3.29)$$

On the other hand, a series electrical resonant circuit consists of an inductor  $L_s$ , a capacitor  $C_s$  and a resistor  $R_s$  under a driven voltage  $v=V\sin\omega t$  is shown in Figure 3.12,

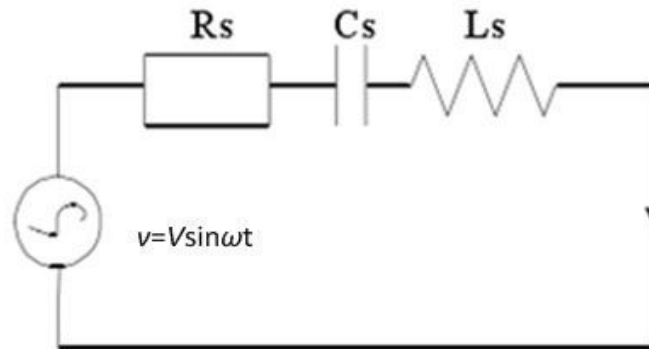


Figure 3. 12: An ideal series RLC electrical resonant circuit

The response function for this  $LCR$  circuit can be easily obtained in [34] as:

$$V = j\omega L_s I + \frac{1}{j\omega C_s} I + R_s X \quad (3.30)$$

By comparing equations (3.29) and (3.30), the analogy between these two systems exists as the elements in a lumped electrical circuit can physically represent the mechanical elements such as its mass, stiffness and damping. The corresponding elements between the two domains are listed in Table 7.

Table 7: Corresponding elements between mechanical and electrical domain

<b>Mechanical Variable</b>	<b>Electrical Variable</b>
Force, $F$	Voltage, $V$
Mass, $m$	Inductance, $L$
Stiffness <sup>-1</sup> , $k^{-1}$	Capacitance, $C$
Damping, $c$	Resistance, $R$
Displacement, $x$	Charge, $q$

With Table 7, the mechanical behaviors can be modeled and solved with an equivalent electric circuit.

### 3.4.2 The Equivalent Electrical Circuit

Once an equivalent electric circuit is modeled and solved with mature circuit theory, many commercial software packages, such as SPICE and ADS, are available to analyze the modeled circuit. As a result, the equivalent circuit method implemented into electromechanical systems lends itself to a particular way to visualize the MEMS system. It may also be used in further analysis and investigation of the effects of connecting subsystems or making modifications to the mechanical structures.

To model the equivalent electrical circuit with a direct analogy, a converting coefficient is needed to present the correspondence between the mechanical and electrical models [31]. In equation (3.13),  $V_{dc} \frac{\partial C}{\partial Z}$ , which illustrates the energy transformation through the transducer capacitor, completely satisfies our demand and can be seen as the transformer coefficient between the force  $F$  and the AC voltage  $V_{in}$ . By implementing the analogy using this transformer coefficient, denoted by  $\eta$ , an equivalent series  $LCR$  circuit is able to be modeled for the single resonator, as shown in Figure 3.12, with element values given by:

$$L_x = \frac{M_r}{\eta}, \quad C_x = \frac{\eta}{K_r}, \quad R_x = \frac{c_r}{\eta} = \frac{\sqrt{M_r K_r}}{Q_0 \eta} \quad (3.31)$$

where  $M_r$ ,  $K_r$ , and  $C_r$  are the equivalent lumped mass, stiffness and damping coefficient, respectively, which can be obtained in the above equation.

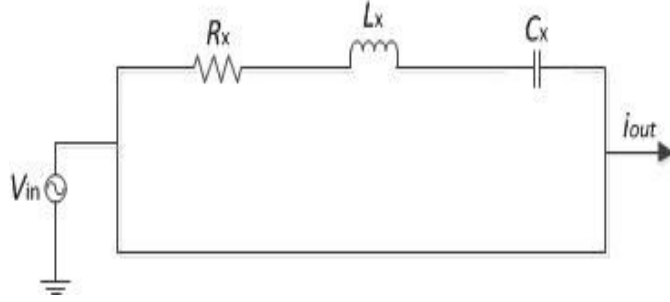


Figure 3. 13: Equivalent lumped circuit for a single resonator

Knowing that the amplitude of displacement at each point on the beam is small, the transformation coefficient  $\eta$  is approximately given by:

$$\eta = \frac{F}{V_{in}} = V_{ac} \frac{\partial C}{\partial Z} \approx V_{ac} \frac{\epsilon_0 W_r W_e}{g_0^2} \quad (3.32)$$

From equation (3.32), we can see  $\eta$  strongly depends on the overlap capacitive parameters, such as  $W_e$ ,  $W_r$  and gap spacing  $g_0$ .

To specify the damping on which the dynamic behavior of the system greatly depends, gravity or inertia damping effects can be neglected for the micro scale structures. However, the effects of the surrounding air, such as friction, play an important role when the micro-device is in motion. Assuming the operation occurs in a vacuum atmosphere, air damping on the resonator performance can ideally be ignored in the modeling. Therefore the complete small-signal electrical equivalent circuits of the system, including the readout circuit, are able to be built and simulated in Agilent ADS [35] as shown in Figure 3.13. Lumped mass, stiffness solved by equation (3.15)

and equation (3.16) and the corresponding electric parameters for designed UW-MEMS and PolyMUMPs micro-resonators are listed in Table 8 and 9.

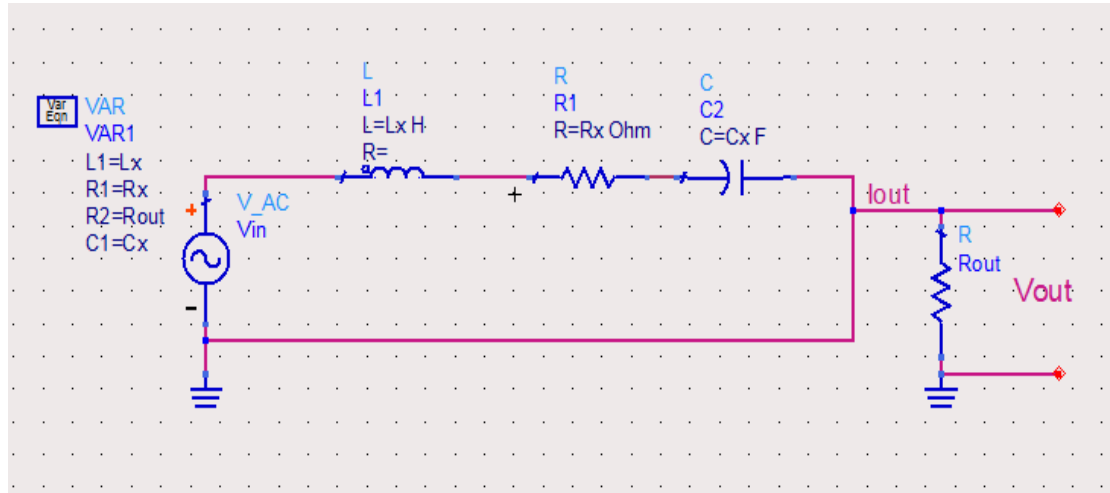


Figure 3. 14: Schematic of an equivalent lumped circuit in ADS

Table 8: Equivalent electrical lumped parameters of UW-MEMS resonator

Parameter	Value	Units	Parameter	Value	Units
V <sub>dc</sub>	25	V	$\eta$	2.42e-9	-
K <sub>r</sub>	227.6	N/m	C <sub>x</sub>	1.06e-11	H
M <sub>r</sub>	8.312e-11	kg	L <sub>x</sub>	3.44e-2	F

Table 9: Equivalent electrical lumped parameters of PolyMUMPs resonator

Parameter	Value	Units	Parameter	Value	Units
V <sub>dc</sub>	40	V	$\eta$	8.22e-9	-
K <sub>r</sub>	3012	N/m	C <sub>x</sub>	2.73e-12	H
M <sub>r</sub>	6.232e-12	kg	L <sub>x</sub>	7.58e-3	F

Figure 3.15 and Figure 3.16 show the simulated transfer function in the form of output to input ratio ( $V_{out}/V_{in}$ ) of the resonators in the frequency domain by using the parameters listed in above tables. These plots are obtained in ideal conditions assuming that the resonators are operating in a vacuum ( $R_x$  very small) and readout resistance  $R_{out}$  is  $50 \Omega$ .

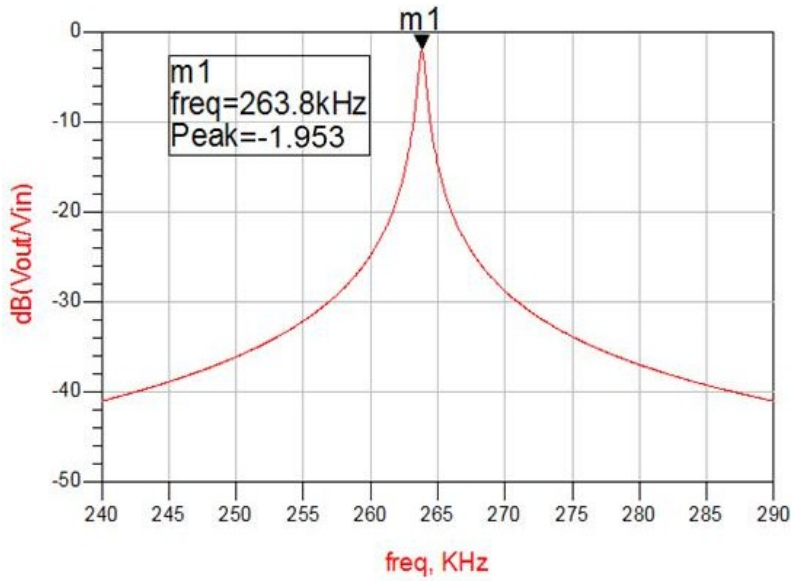


Figure 3. 15: Frequency characteristic of the 263.6 kHz UW-MEMS resonator

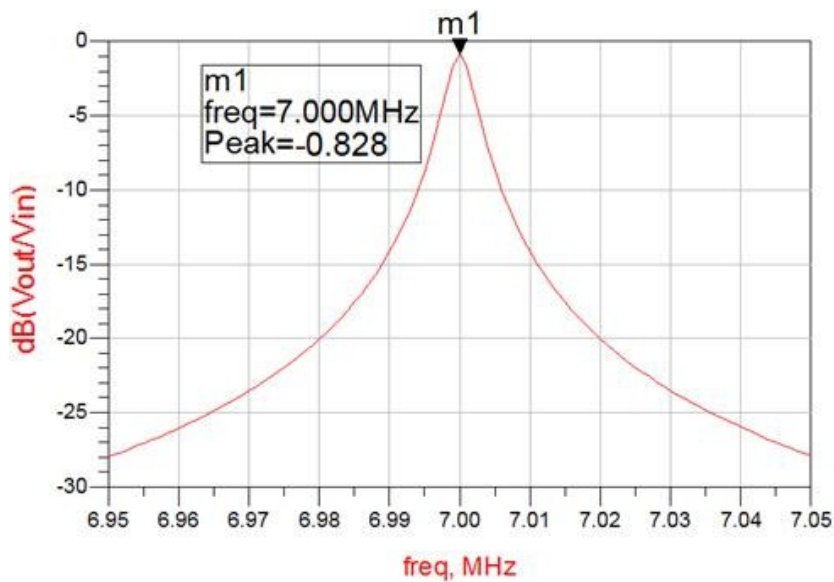


Figure 3. 16: Frequency characteristic of the 7 MHz PolyMUMPs resonator

### **3.5 SUMMARY**

This chapter describes the structure design and operating principle of the free-free beam micromechanical resonator. The parameters involved in the design are presented through well-established beam and vibration theory. Electromechanical coupling effect in operation is analyzed as well. An equivalent electrical circuit is modeled to simulate the electrical characteristics of the resonator by mechanic-to-electric analogy method.

## **CHAPTER 4    FINITE ELEMENT ANALYSIS**

In this chapter, finite element analysis (FEA) is used to simulate the resonator response characteristics.

### **4.1 INTRODUCTION TO FEA**

The finite element method (FEM) originated from the need for solving complex elasticity and structural analysis problems. It is a numerical technique for finding approximate solutions to partial differential equations (PDE) and their systems, as well as integral equations [36]. In simple terms, FEM (practical application often known as finite element analysis (FEA)) is a method that divides up a very complicated problem into small elements (each element is discrete object resulting from meshing), solve for each element and obtain the complete solution by collecting individual solutions through inter-elemental boundaries allowing for continuity. Typically, it is an attractive choice for solving complicated multi-domain problems which provides us a useful tool in MEMS related research.

A commercially available FEA software solver, COMSOL Multiphysics 4.2a [37], is used for finite element analysis in this thesis. In it, A 2D or 3D geometry model is built to represent the physical system of the resonator. All dimensional parameters are in micro scale and material properties are added to the objective structures in the simulation. An electromechanic simulation is performed to determine the response of the resonator due to electrostatic actuation. The solver solves the electrostatic equation in the surrounding air domain using the arbitrary “Moving Mesh (ALE)” method to account for the geometry deflection associated with the beam deformation.

## 4.2 ANALYSIS FOR UW-MEMS RESONATOR

With the design parameters of Table 5, a resonator is modeled in 3D. For UW-MEMS process, the structural material is gold (Au) and its properties are specified in Table 10.

Table 10: Material properties used in FEA for UW-MEMS resonator

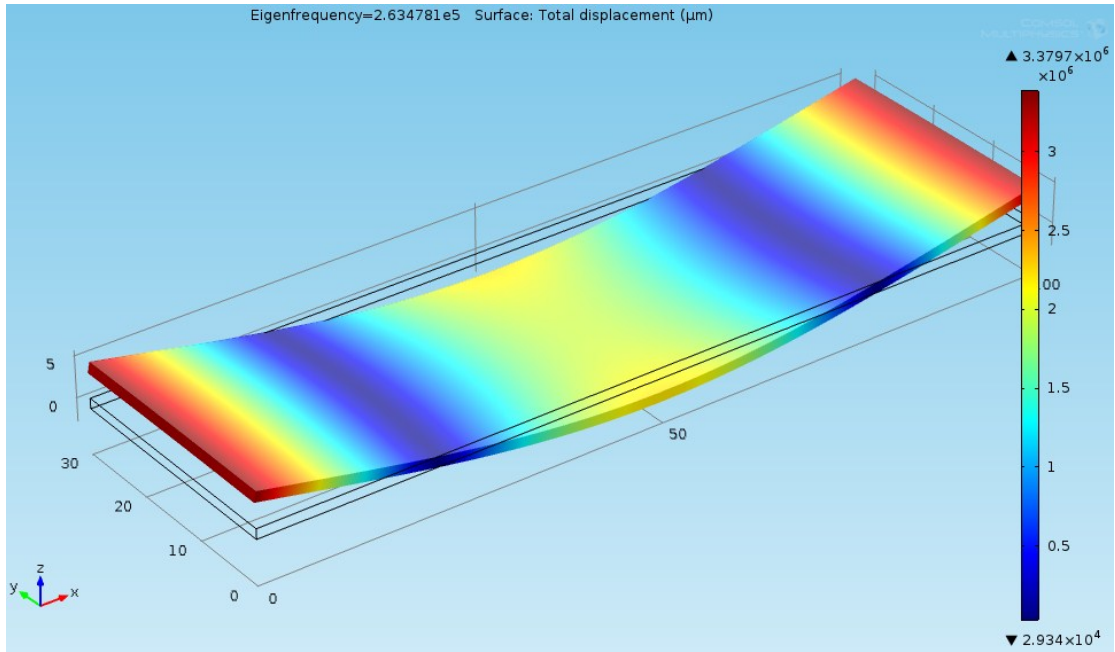
	Property	Name	Value	Unit
✓	Density	rho	19300	kg/m <sup>3</sup>
✓	Young's modulus	E	79.5e9	Pa
✓	Poisson's ratio	nu	0.44	1
	Electrical conductivity	sigma	45.6e6	S/m
	Coefficient of thermal expansion	alpha	14.2e-6	1/K
	Heat capacity at constant pressure	Cp	129	J/(kg*K)
	Thermal conductivity	k	317	W/(m*K)

Before running the simulation, meshing for the elements should be strategically defined to validate the accuracy of the results. In general, the smaller elemental size is defined, the more accurate results will be obtained at a cost of longer solving time. In this chapter, all the FEA simulations are performed with extremely fine meshing to ensure the reliability of the results. A 100  $\mu\text{m}$  beam micro-resonator based on the study described in previous chapters is simulated in sequence. Detailed steps are illustrated in the Appendix A.

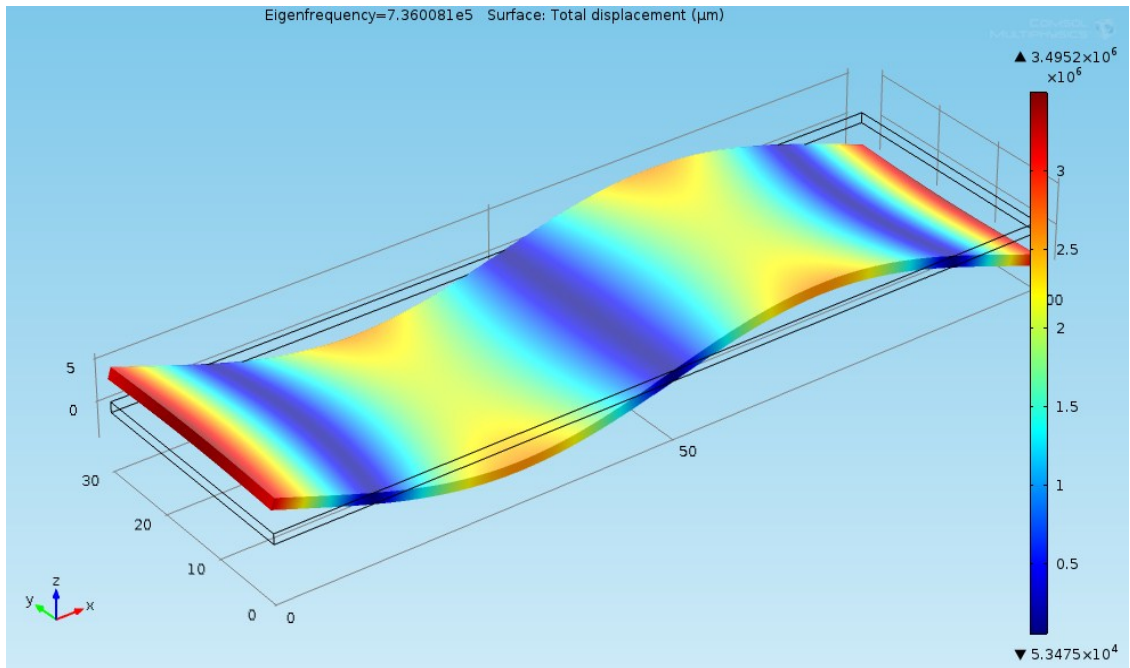
### 4.2.1 Modal Analysis

Modal analysis is performed to determine vibration characteristics (like natural frequency and mode shapes) of the beam. This is also served as a starting point for other analysis. The COMSOL eigenfrequency solver is used to analyze the first three

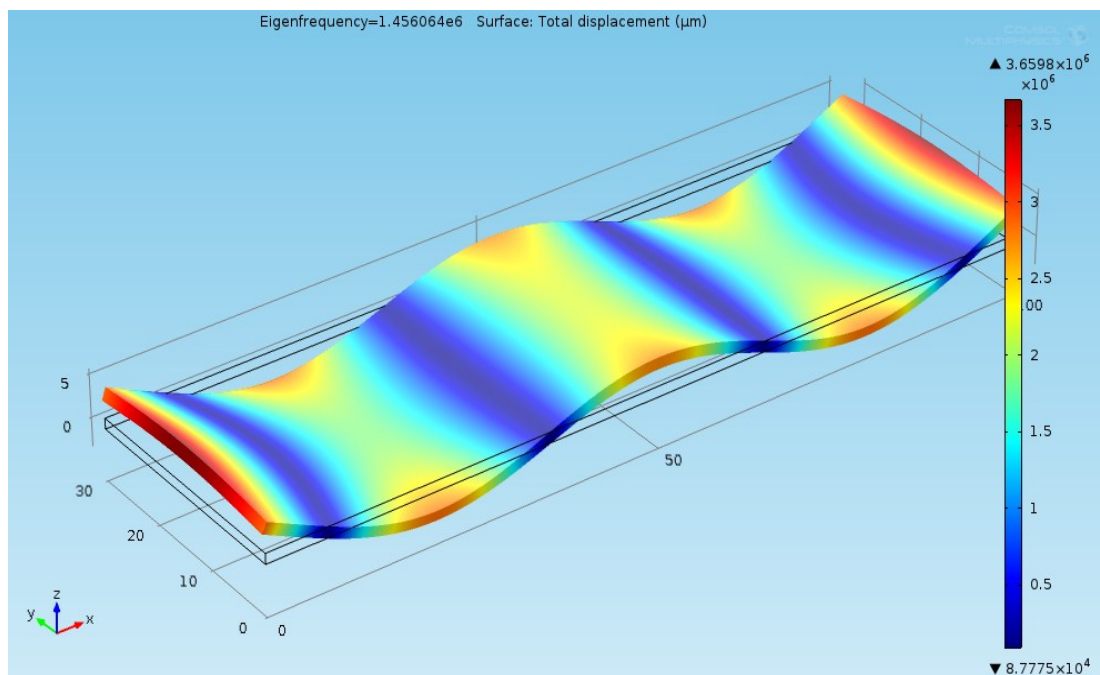
harmonic mode shapes shown in Figure 4.1. The modal frequencies are indicated in the figures with the legend colors representing the relative vertical displacement magnitude.



(a)



(b)



(c)

Figure 4. 1: Modal analysis of the first three harmonic resonance modes of the FF-beam: (a) First mode with frequency of 263.5 kHz, (b) Second mode with frequency of 736 kHz, (b) Third mode with frequency of 1.456 MHz

The first mode in operation is the one we are interested in. As we can see from Figure 4.1, the fundamental vibration mode for a 100 μm free-free beam has the expected shape and the natural frequency of 263.5 kHz. The frequency is very close to the theoretical calculation as listed in Table 5. Moreover, from the displacement plot of the beam in the z direction shown in Figure 4.2, we verify the positions of nodal points as derived from the normalized mode shape function in Figure 3.5.

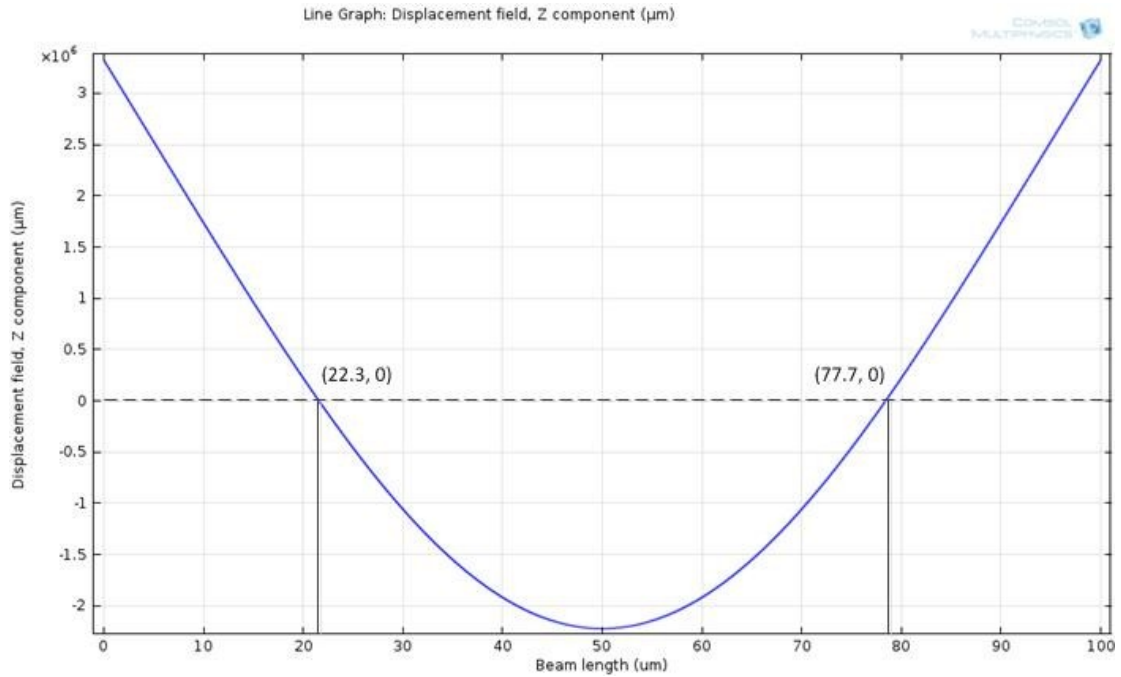


Figure 4. 2: Simulated curve of the first mode shape for a 100  $\mu\text{m}$  free-free beam

#### 4.2.2 Static Analysis

After generating a vacuum air box surrounding a simplified resonator structure, 25 V DC bias is applied to the bottom electrode while the resonator is grounded. The software solves the displacement of the beam by calculating the electric field in the surrounding air. As the beam bends, the geometry of the air changes continuously and the Moving Mesh (ALE) model will take this displacement into account when computing the electrostatic force. Finally, the beam will reach to an equilibrium position and displacement can be obtained. The electric potential distribution and contours between the air gap are shown in Figure 4.3. The fringing fields extend into the gap either side of the resonator. It should be noted that the surface of the resonator is assumed to be perfectly grounded.

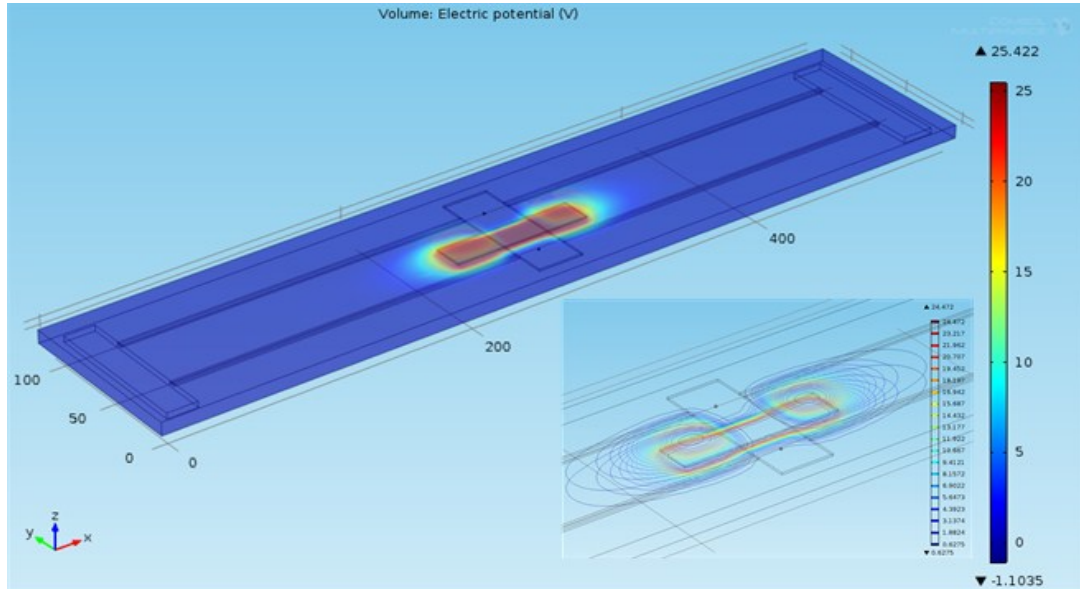


Figure 4. 3: Electric potential field and contours in the gap between the grounded resonator and the biased driving electrode

Figure 4.4 shows the vertical displacement of the structure with the applied DC bias of 25 V. The maximum displacement solved by FEA is 22.4 nm, which differs from the theoretical solution 21 nm of equation (3.23) by 6.25%.

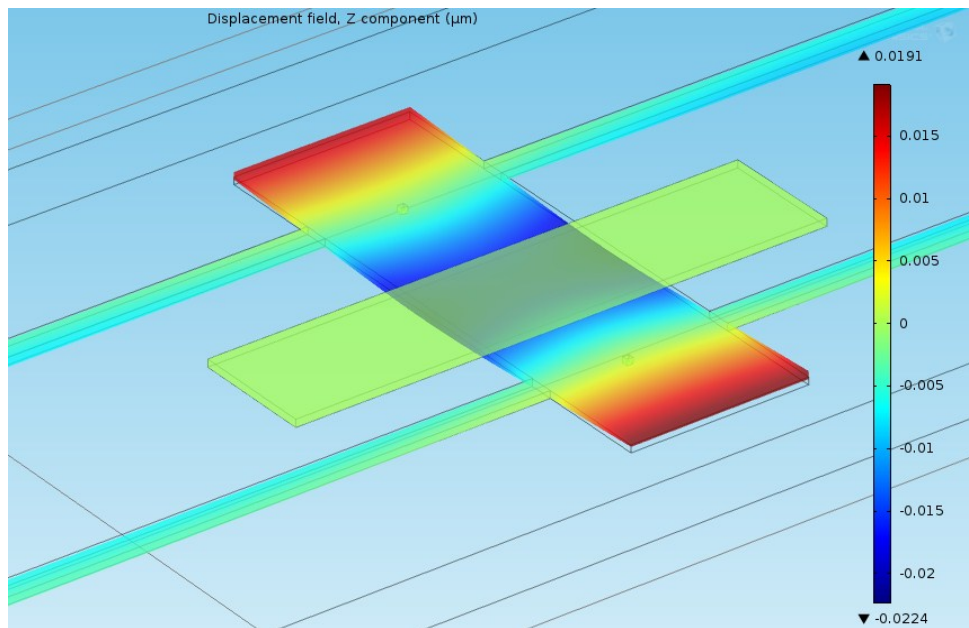


Figure 4. 4: Displacement of the resonator under DC bias of 25 V

The static positions under various applied voltages (from 15 volts to 30 volts with a step of 5 volts) are simulated by COMSOL parametric sweep solver, presented in Figure 4.5.

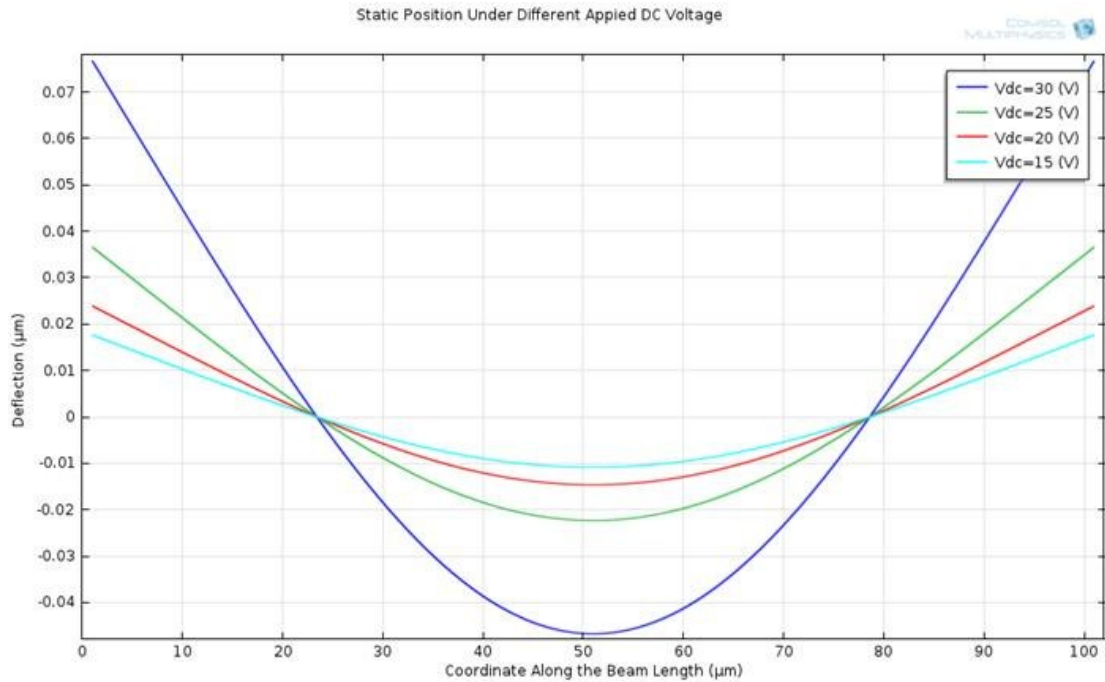


Figure 4. 5: Displacements of the UW-MEMS beam under different DC bias voltage

It is apparent that the maximum deflection of the resonator occurs at the midpoint of the beam and will become bigger as the applied voltage increases.

### 4.2.3 Dynamic Response Analysis

Dynamic response analysis is modeled to determine the response of the resonator with excitation that varies sinusoidally with time. In simulation, a 100 mV AC signal is added to the stationary model as a harmonic perturbation to the DC bias, and COMSOL solves the dynamic response of the system by calculating the magnitude of

displacement in the frequency domain. Figure 4.6 shows the response of the fundamental mode of the resonator at the center point of beam.

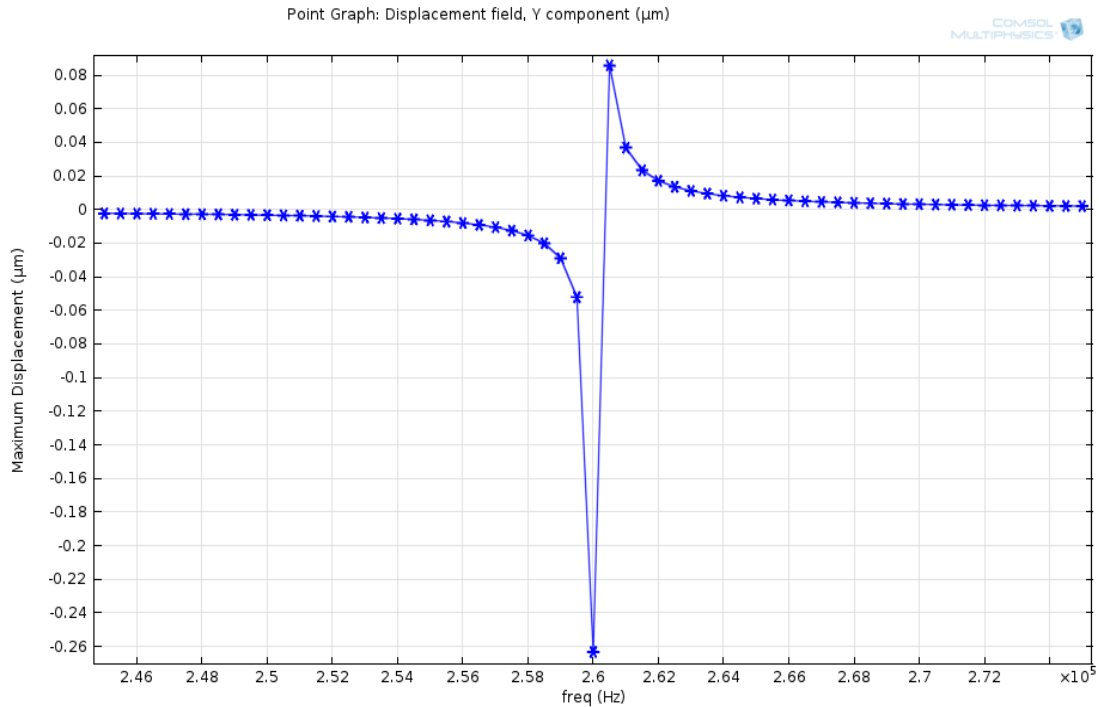


Figure 4. 6: Dynamic response of the fundamental mode of the resonator

As seen in the above plot, a clear vibration at the resonance frequency is seen. The maximum vibrating magnitude is simulated as 0.34  $\mu\text{m}$ . Besides, the center frequency turns out to be around 260.5 kHz under the condition of 25 volts DC bias due to electrical stiffness softening effect which can reduce the operating frequency of the resonator. The relationship between applied voltage and the center frequency is shown in Figure 4.7.

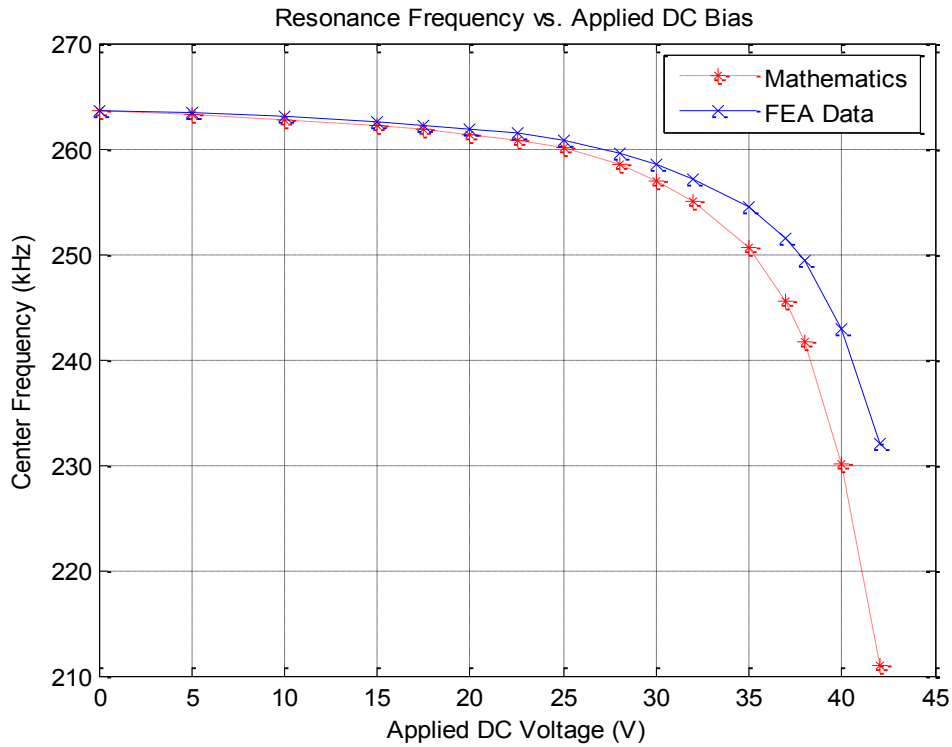


Figure 4. 7: Resonance frequency shown against the applied DC voltage bias

As seen, there are some differences between the theoretical and FEA results. The reason might be attributed to different gap spacing solution when solving equation (3.23) because the fringing effect and beam bending are all taken into account in FEA simulation. When the resonance frequency of the system approaches zero due to the stiffness softening effect at the pull-in position, the catastrophic pull-in voltage solved by COMSOL turns out to be 50.1 V, which is 4.2 V larger than the analytical result.

### 4.3 ANALYSIS FOR POLYMUMPs RESONATOR

FEA simulation is carried out for the PolyMUMPs resonator following the same procedure as for the UW-MEMS one. The structural material is changed to polysilicon with properties listed in Table 12. A 49.4  $\mu\text{m}$  beam resonator with center

frequency of 7 MHz is taken as an example and dimensional parameters in Table 3.6 are applied.

Table 11: Material properties used in FEA for PolyMUMPs resonator

Property	Name	Value	Unit
✓ Relative permittivity	epsilon <sub>r</sub>	4.5	1
✓ Density	rho	2330	kg/m <sup>3</sup>
✓ Young's modulus	E	160e9	Pa
✓ Poisson's ratio	nu	0.22	1
Coefficient of thermal expansion	alpha	2.6e-6	1/K
Heat capacity at constant pressure	C <sub>p</sub>	678	J/(kg*K)
Thermal conductivity	k	34	W/(m*K)

The fundamental mode shape and the eigenfrequency analysis of the beam are presented in Figure 4.8. Analysis of the resonators with the support structures are presented in Figure 4.9 for comparison.

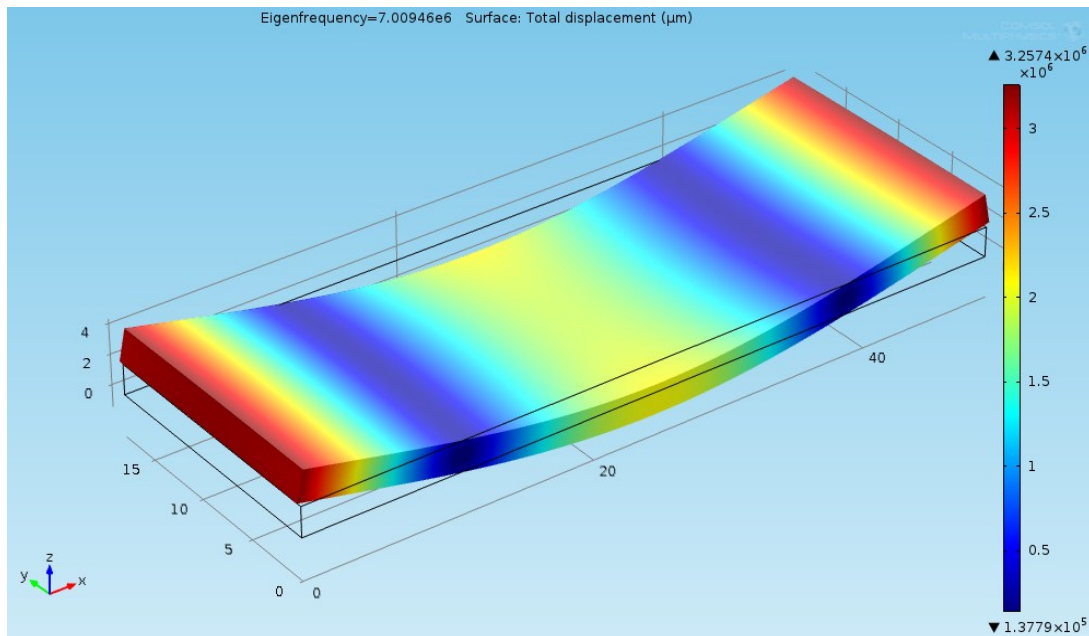
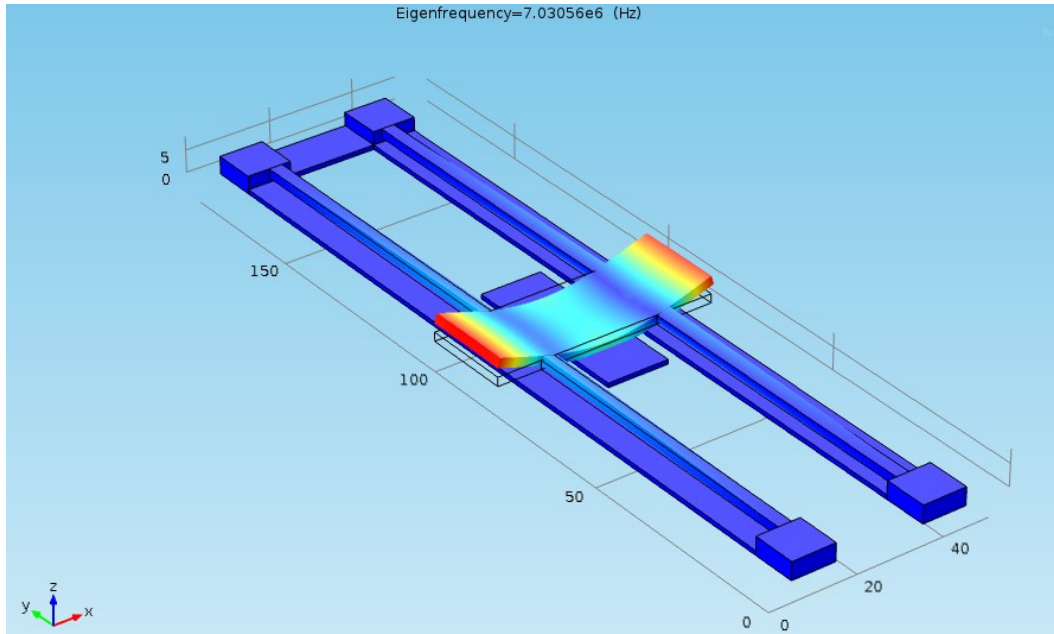


Figure 4. 8: Fundamental mode shape of a 49.4 µm free-free beam with eigenfrequency of 7.01 MHz



(b)

Figure 4. 9: Mode shape of the PolyMUMPs resonator with the support structures, the eigenfrequency of which is 7.03 MHz

We can observe that the fundamental mode shapes of the free-free beam in above two figures are the same and the eigenfrequency obtained with and without support structures show little difference (0.28% calculated). This demonstrates that the support structures connected at nodal points of the free-free beam have negligible impact on the vibration mode shape and resonance frequency.

The static analysis of PolyMUMPs resonator under DC bias is similar to the one shown in Figure 4.4. However, different static position tends to be obtained because of the distinct material properties and structural dimensions. In terms of this 49.4  $\mu\text{m}$  beam resonator, displacement positions under various applied voltages (from 10 volts to 40 volts) are presented in Figure 4.10.

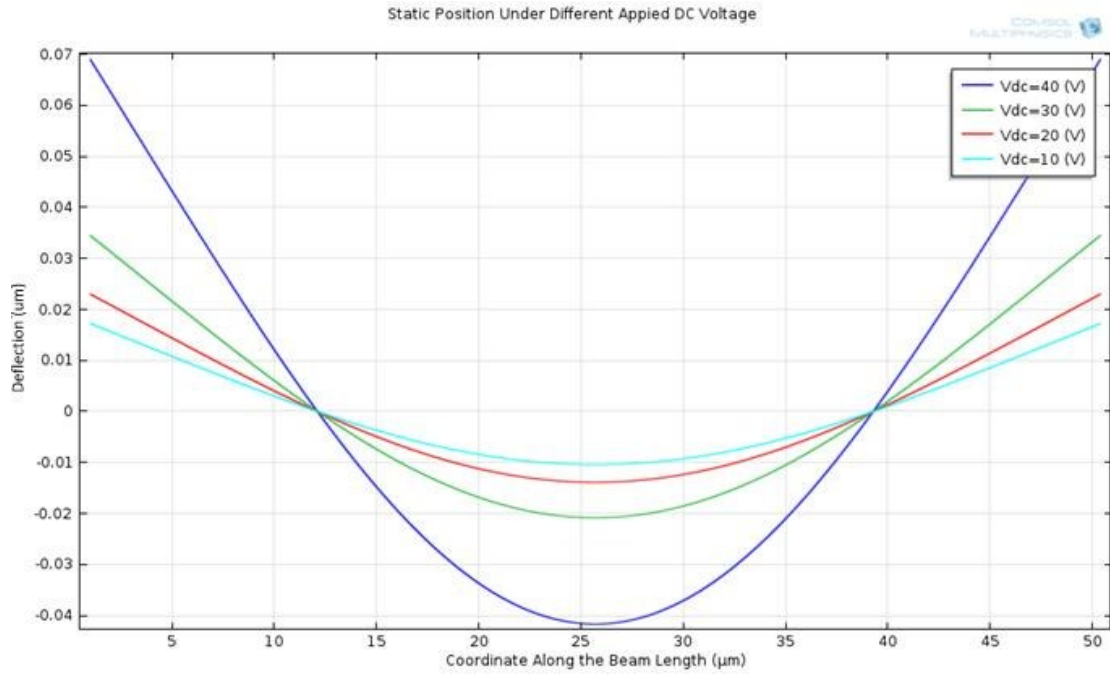


Figure 4. 10: Displacements of the beam under different DC bias voltage

Dynamic response is also simulated under the condition of 40 V DC bias and 100 mV AC excitation. The plot of the response is illustrated in Figure 4.11.

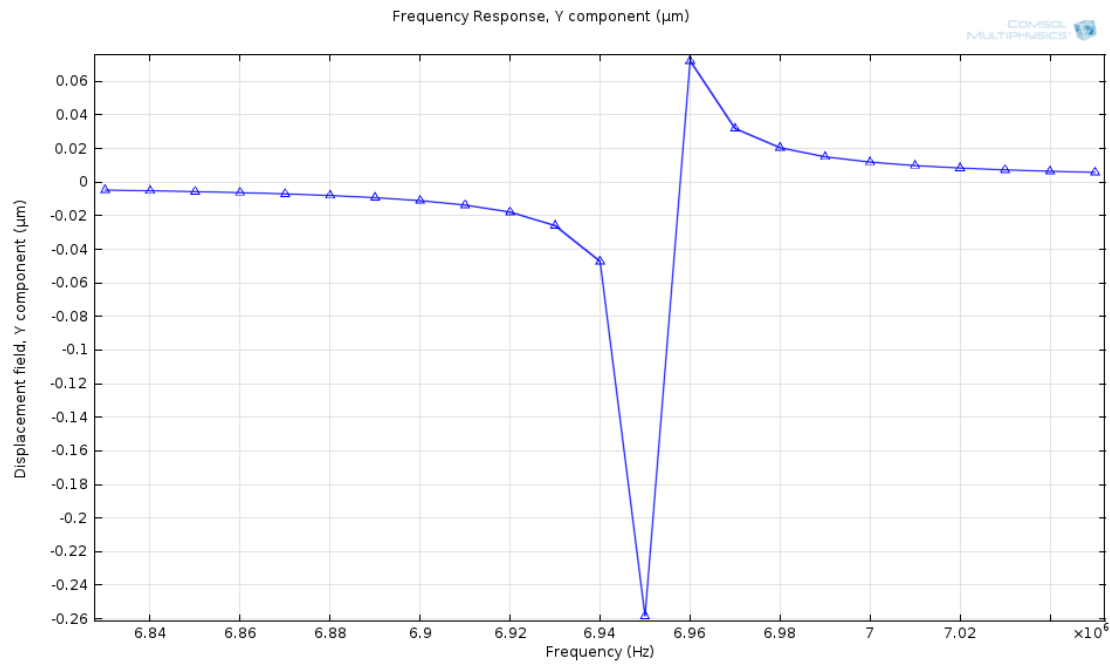


Figure 4. 11: Dynamic response of the 49.4 μm beam PolyMUMPs resonator

As we can see from Figure 4.11, the frequency shifting phenomenon can be still observed. The resonance frequency of this PolyMUMPs resonator reduces from 7 MHz to 6.95 MHz under the 40 V bias.

#### **4.4 SUMMARY**

The finite element analysis (FEA) method is performed in this chapter to analyze the behavioral characteristics of the designed resonators. Modal, static and dynamic analyses are simulated and the results agree with the theoretical values.

## CHAPTER 5 EXPERIMENTAL IMPLEMENTATION

Experimental measurements of a fabricated device are performed to verify that the resonator is performing properly according to the design criteria. This chapter describes the experimental setups and testing results. Static, dynamic response and electrical testing are carried out. The experimental are compared with theoretical and simulation results and difference between them are discussed

### 5.1 STATIC AND DYNAMIC TESTING OF UW-MEMS RESONATOR

Several free-free beam micro-resonators are fabricated using both UW-MEMS process and PolyMUMPs through CMC Microsystems. Figure 5.1 is a photograph of a fabricated 84-pins PGA packaged chips with wire-bounded inside.

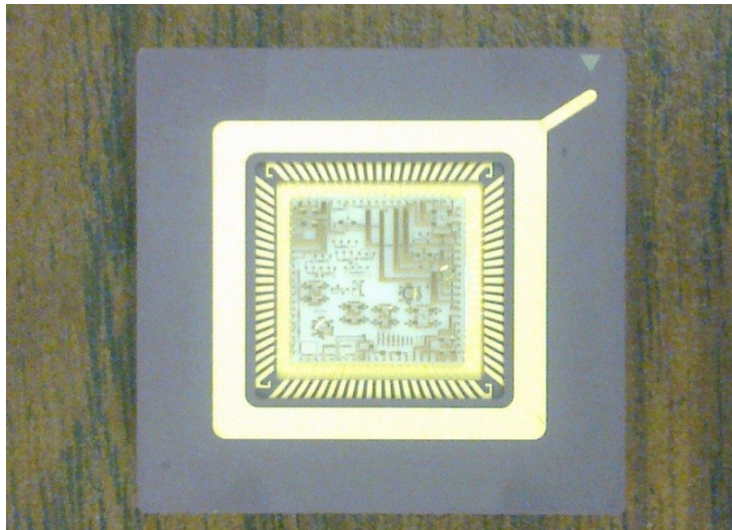


Figure 5. 1: Photograph of a UW-MEMS packaged chip

### 5.1.1 Experimental Setup

The surface profile, static measurement and the dynamic performance of the resonators are measured using a Veeco NT 9100 In-Motion System shown in Figure 5.3. A DC bias is applied to the bottom electrode using a power supply. The profiler has a built-in signal generator which can implement an AC excitation and the ground is applied to the resonator structure.

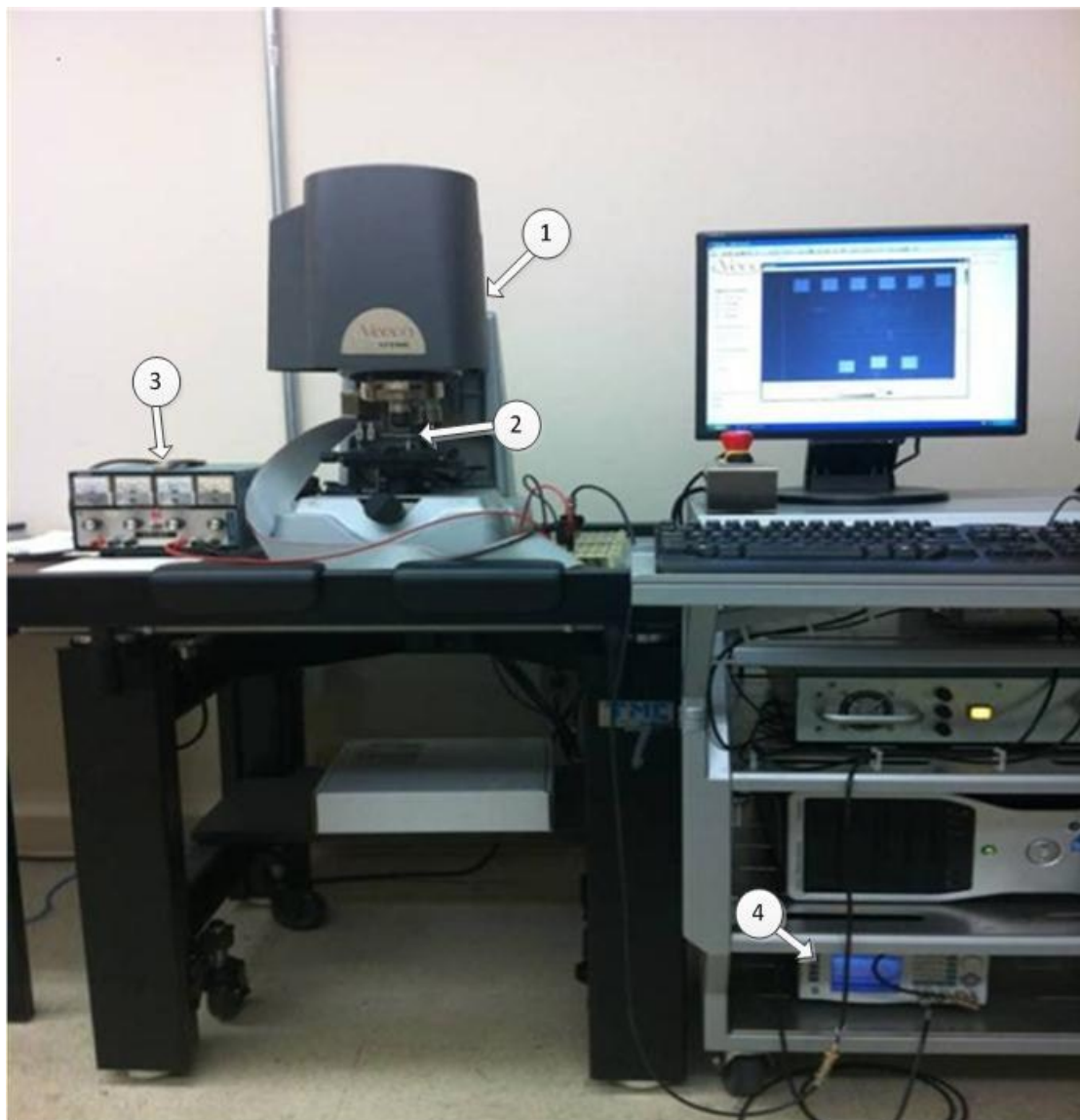


Figure 5. 2: Photograph of the dynamic experimental setup: ① Veeco NT 9100 optical profiler, ② Packaged chip, ③ DC power supply, ④ AC signal generator,

### 5.1.2 Static Measurement

Veeco NT-9100 optical profiler is an interferometric microscope-based 3D, non-contact, surface measurement system that is used to carry out the structural measurements [38]. In the static measurement, NT-9100 is used to capture images of MEMS chips and surface topography. The height data of the fabricated resonator are taken with reference to a flat substrate. Figure 5.3 shows a 3D top view of the 100  $\mu\text{m}$  beam resonator with traces and bonding pads.

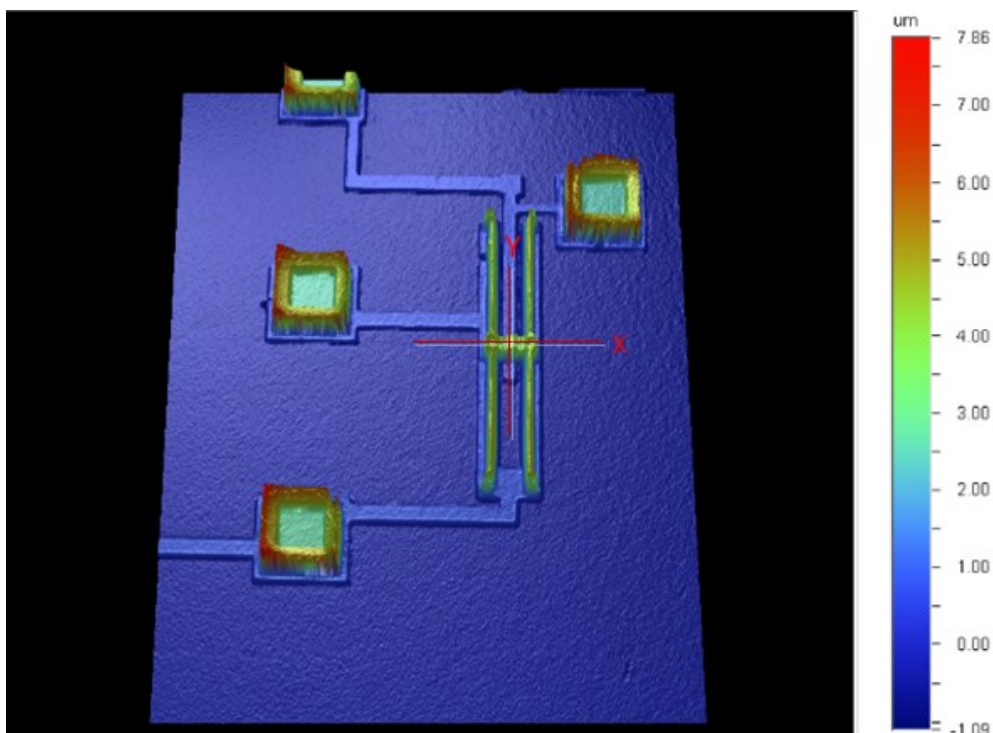


Figure 5. 3: 3D view of the UW-MEMS resonator

The 2D profiles in Figure 5.4 and 5.5 present a clear picture of the surface topography of the resonator when no voltage is applied. The Z-distance from the bottom electrode surface to the beam surface is read as 3.75  $\mu\text{m}$  from Figure 5.5, which exactly equals to the sacrificial layers thickness (2.5  $\mu\text{m}$ ) plus structural gold thickness (1.25  $\mu\text{m}$ ).

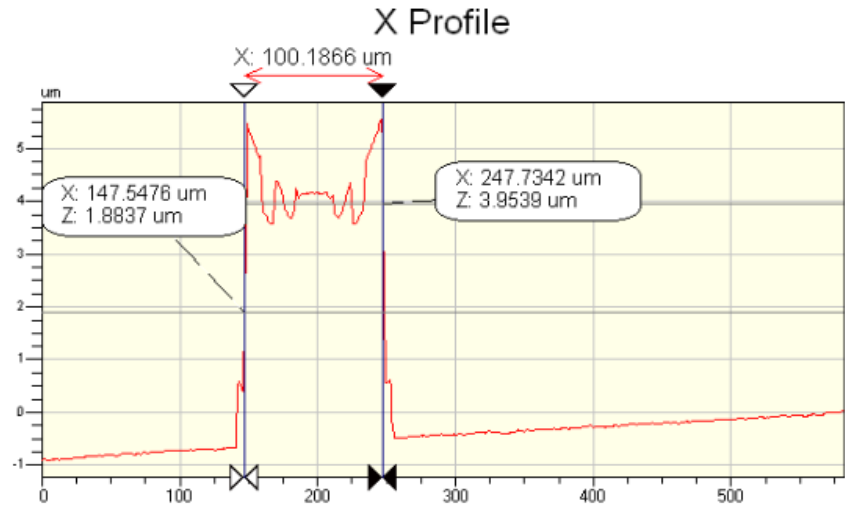


Figure 5. 4: 2D surface profile along the length of the resonator

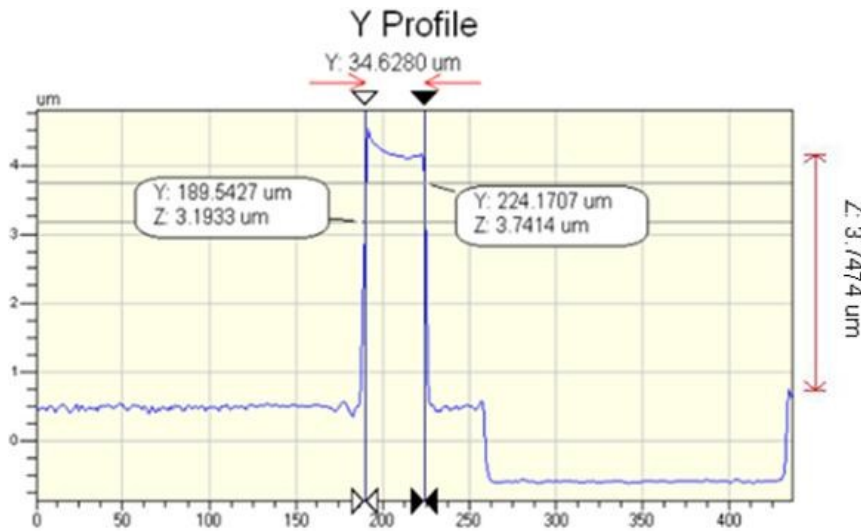


Figure 5. 5: 2D surface profile along the width of the resonator

As shown in above figures, the NT-9100 profiler software can display the measured length and width of the beam, respectively. Apparently, the resonator is not completely flat and there is a little curvature of the beam mainly due to the residual stress induced by the process.

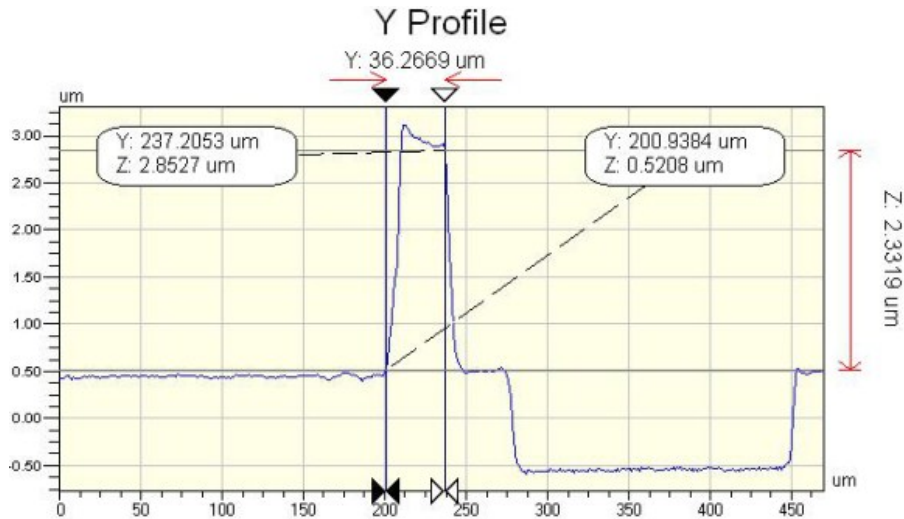


Figure 5. 6: 2D surface profile along the width of the resonator under DC bias

Figure 5.6 is a Y Profile of the resonator under a 25 V DC bias. By comparison with Figure 5.5, the Z-distance from the bottom electrode surface to the beam surface changes to 2.33  $\mu\text{m}$  (close to the dimple height 1  $\mu\text{m}$  plus gold thickness 1.25  $\mu\text{m}$ ) which indicates that the beam structure has dropped down by the electrostatic attraction and sit upon the dimples as expected.

### 5.1.3 Dynamic Testing

The dynamic performance of the device is tested using the setup as shown in Figure 5.2. A 25 V DC voltage is applied to the electrode and a frequency sweep from 200 kHz to 400 kHz with step of 1 kHz is performed with a sine wave of 100 mV amplitude. A peak is detected around 320 kHz. Another frequency sweep with step of 0.1 kHz is performed again from 310 kHz to 330 kHz. From Figure 5.7, the actual resonance frequency occurred at 323.7 kHz.

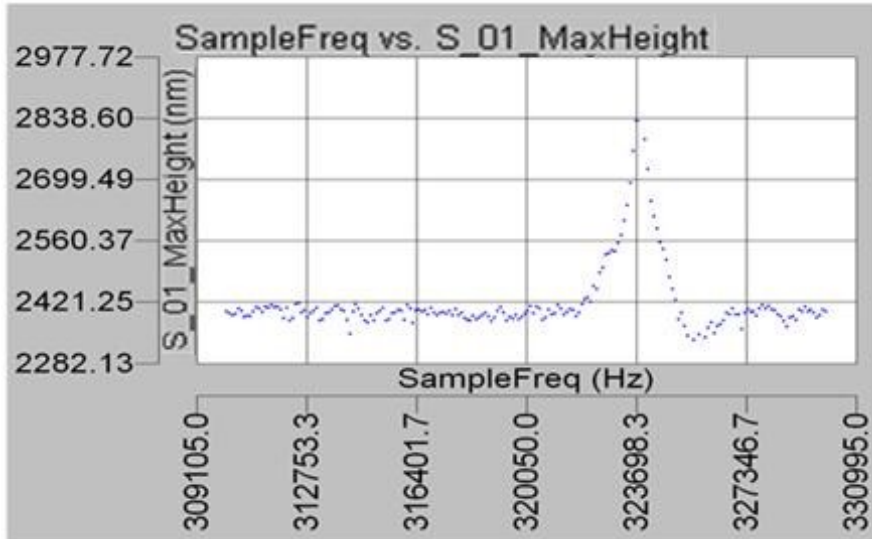


Figure 5. 7: Dynamic testing for resonance performance

The quality factor (Q), which describes how fast a system decays or equivalently a measure of the relationship between stored energy and rate of energy dissipation, is a very important parameter for resonator [25]. Higher Q indicates a lower rate of energy loss relative to the stored energy. And it can be determined by characterizing its bandwidth relative to its center frequency as shown in Figure 5.8.

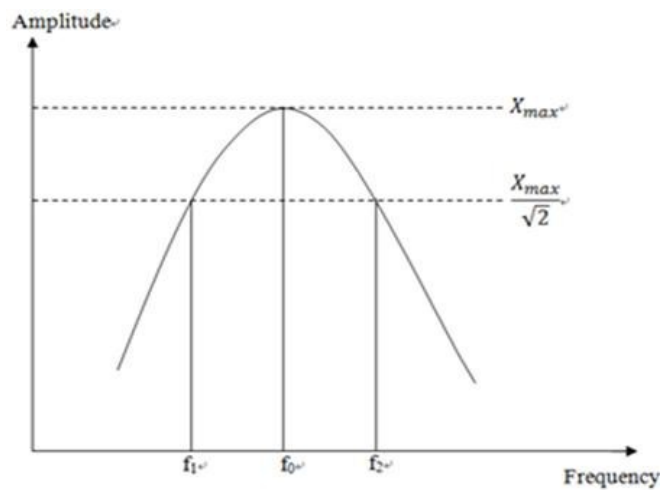


Figure 5. 8: Quality factor determination

The quality factor of this 100  $\mu\text{m}$  free-free beam resonator is calculated from

experimental results in Figure 5.7 as:

$$Q_f = \frac{f_0}{\Delta f} = \frac{f_0}{f_2 - f_1} = \frac{323.69 \text{ KHz}}{(323.55 - 323.8) \text{ KHz}} = 1294.8 \quad (5.1)$$

where  $f_0$  is the center frequency and  $\Delta f$  is the bandwidth of oscillation.

## 5.2 ELECTRICAL TESTING OF UW-MEMS RESONATORS

To obtain the frequency characteristics in electrical domain of the fabricated resonators, a testing system is set up as shown in Figure 5.9. A DC source power supply and AC waveform generator provide the input signal through cables. The output signal is detected and measured by an oscilloscope which probes at a 50  $\Omega$  output resistor. The recorded results are subsequently plotted in the frequency domain as a ratio of  $v_{out}/v_{in}$ .

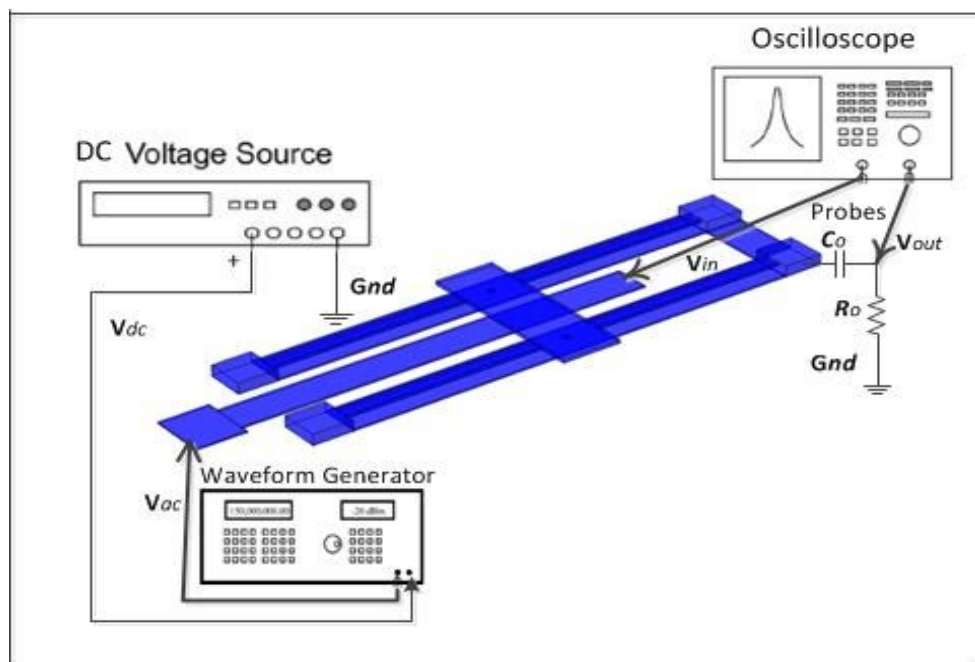


Figure 5. 9: Schematic diagram of the electrical testing

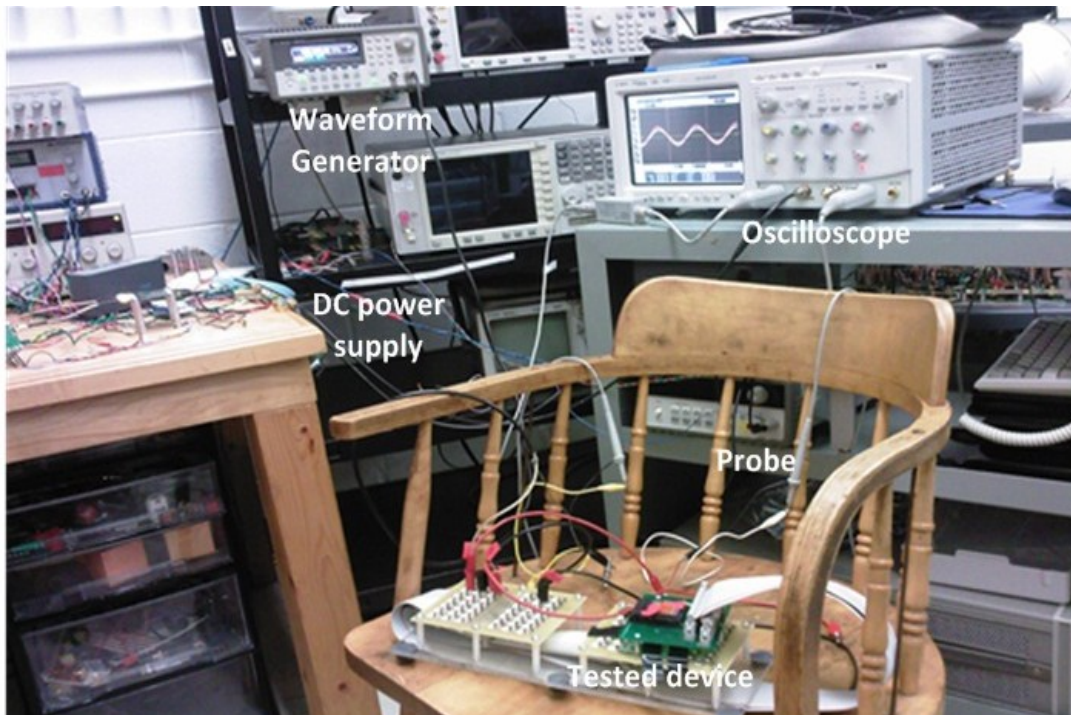


Figure 5. 10: Photograph of the electrical testing setup

Fig. 5.10 presents a photo of the testing setup in the lab environment. A variety of dc and coaxial cables have been used to provide connections.

Since the actual resonance frequency of the device is obtained by previous dynamic testing, the measurement carried out in electrical domain mainly focus on the frequency characteristic around 323.7 kHz. The bias and excitation voltage is the same values as in dynamic measurement and the frequency of the input signal is swept from 322 kHz to 325 kHz by a waveform generator (Agilent 33250A) with a step of 50 Hz.

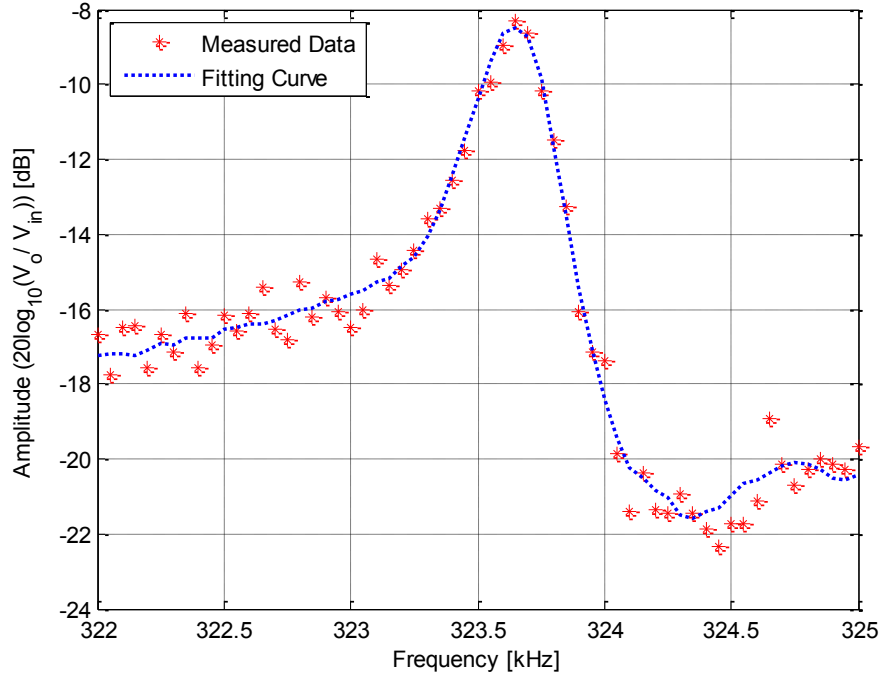


Figure 5. 11: Measured data in electrical testing and plotted fitting curve

The output signal is detected and displayed on the oscilloscope (Agilent Infinium DS081204B) so that the frequency spectrum can be plotted by the measured amplitude ratio of  $v_{out}/v_{in}$ . Figure 5.11 presents the measured data for the 100  $\mu\text{m}$  free-free beam resonator in dB ( $20\log_{10}(v_{out}/v_{in})$ ). A fitted curve is plotted along the scattered points for a straightforward view. Comparing the curve with the electrical simulation plot in Figure 3.15, the curve shapes around the resonance frequency are similar except that the measured result has a higher insertion loss of 8.3 dB because Rx in simulation assumes to be very small. Since 3 dB rolling off should be counted when calculating the quality factor in this situation, Q of the device in electrical testing extracted from this plot turns out to be [34]

$$Q_f = \frac{f_0}{\Delta f_{3dB}} = \frac{323.65 \text{ kHz}}{(323.76 - 323.49) \text{ kHz}} = 1197.3 \quad (5.2)$$

## 5.3 RESULTS AND ANALYSIS

### 5.3.1 Resonance Frequency

Table 12 summarizes and compares the theoretical, simulation and experimental results of the resonance frequency.

Table 12: Comparison between theoretical, simulation and experimental results

	Theoretical	Simulation	Experimental
frequency ( <i>kHz</i> )	263.6	263.5	323.7

As seen in the table, the simulated frequency is very close to the theoretical predictions, however, the measured result turns out to be 18.57% larger than the expected value.

The reason for this discrepancy is mainly due to the fabrication of the UW-MEMS process. First of all, material properties of the gold given by the handbook may not be exactly applicable to the thin film conditions, minor difference in property parameters can lead to distinctly different frequency performance. Also, ideally, the vibrating beam is considered as a flat surface, but the actual structure has some small etching holes on top as shown in Figure 5.4. Besides, the beam itself has a slight curvature mainly caused by the residual stress which is generated from the fabrication process such as physical or chemical vapor deposition, sputtering and electroplating [22]. For dynamic analysis, the presence of etching holes and curvature can affect the effective mass and stiffness of the structure, therefore changing the resonance properties of the system.

Another important factor mustn't be ignored is the impact of the dimples. In FEA

simulation, dimples are centered at the nodal locations along the length of the beam in small dimensions ideally. In reality, however, their finite widths ( $5 \mu\text{m} \times 5 \mu\text{m}$ ) prevent them from acting as true nodal supports [21]. Their existence may in fact introduce additional constrains to the beam during resonance vibration, thus increasing the center frequency of the system.

### 5.3.2 Quality Factor

Quality factor obtained from FEA simulation and the measurement in both dynamic testing and electrical testing are listed in Table 13.

Table 13: Comparison of quality factor between FEA and experimental results

	FEA	Dynamic	Electrical
Quality Factor	2330	1294.8	1197.3

From above table, it is seen that FEA simulation result is much higher than the measured results. This is because a vacuum surrounding is applied in FEA while the measurements are conducted at ambient pressure. Viscous gas damping could also be a major factor that has impact on the measured quality factor. In addition, additional constrains introduced by the finite-width supporting beams and dimples during vibration may lead to energy losses, lowering the quality factor. Other factors, such as electrical parasitic losses, could also be accounted.

## **5.4 SUMMARY**

This chapter describes the experimental methodology and the setup. The fabricated UW-MEMS resonators are tested for static, dynamic and electrical performances. Theoretical, FEA simulation and experimental results are compared and analyzed. Explanations on the differences among the results of theory, simulations and measurement are provided.

The static measurement is performed for the 49.4  $\mu\text{m}$  free-free beam PolyMUMPs resonator and figures are shown in Appendix B. Unfortunately, the In-Motion measurement of the Veeco NT-9100 System can only run the frequency sweep up to 5 MHz, which means the dynamic testing of the PolyMUMPs micro-resonator is unable to perform and will be left as a future work.

## **CHAPTER 6 CONCLUSIONS AND FUTURE WORK**

In this chapter, the conclusion of the research and the thesis contribution are summarized. Future work on improving the testing of the device and some recommendations for modification of the resonator are given.

### **6.1 CONCLUSIONS**

In this thesis, the flexural mode free-free beam MEMS resonator is studied. An introduction and a literature review are presented. Two different processes, UW-MEMS process and PolyMUMPs, are used to fabricate the micro-resonators. Detailed fabrication steps of these surface micromachining processes are introduced. Through the analytical calculation and FEM analysis described, the working principle and dimensional parameters of the micro-resonators are determined and simulated by COMSOL 4.2a. A mechanic-to-electric analogy approach is implemented to study the multi-domain physics of the resonators, which can be utilized effectively for design and optimization of MEMS resonators.

A 100  $\mu\text{m}$  free-free beam UW-MEMS resonator is designed with resonant frequency of 263.6 kHz. Finite element analysis simulations, such as vibration mode shape, resonance frequency, static displacement, stiffness soften effect and pull-in voltage agrees well with the theoretical model. The static, dynamic and electrical testing are carried out. Measured resonance frequency is close to 323.7 kHz and the quality factor is 1295. Discrepancy among the theoretical, simulation and experimental results is discussed.

Another 49.4  $\mu\text{m}$  PolyMUMPs resonator with frequency of 7 MHz is designed and studied as well. FEA simulations and static testing are performed.

## **6.2 FUTURE WORK**

The most important future work is the improvement of the experimental setup and to continue the testing of PolyMUMPs resonator. In general, the tests should be carried out in a vacuum chamber to eliminate the effect of air damping on the resonance performance. Also, it is recommended that a lose-die chip containing resonator is embedded onto a custom designed pc-board and tested by the spectrum network analyzer. In doing so, a much higher range of frequency characteristics up to GHz is obtainable.

Another challenge is that the structures presented in this thesis are all fabricated through the process which is for general MEMS designs. Though they are commercially conveniently available, limitations such as minimal dimension and spacing distance dictated by the process, lead to the difficulty to push the operation frequency to higher range. As a result, a specific fabrication process needs to be developed for the better performance of the MEMS resonators.

Reliability of RF-MEMS components seems to be another critical issue that needs to be resolved before they receive wider acceptance by the market [39]. A thorough investigation on reliability, life cycle, thermal stability, fracture and fatigue of these resonators has to be conducted in the future to prove their suitability in oscillation and filtering applications.

## BIBLIOGRAPHY

- [1] C. Liu, *Foundation of MEMS*, Prentice Hall, 2005, pp. 1-8.
- [2] C. T. Leondes, *MEMS/NEMS Handbook*, Springer, 2007, pp 23-25.
- [3] N. Maluf, *An Introduction to Microelectromechanical Systems Engineering*, Artech House, Boston, 2000.
- [4] H. Baltes, O. Brand, G. K. Fedder, C. Hierold, J. G. Korvink, O. Tabata, *CMOS-MEMS*, John Wiley & Sons, March 2005.
- [5] R. A. Johnson, *Mechanical Filters in Electronics*, New York: Wiley, 1983.
- [6] G. M. Rebeiz, *RF MEMS Theory, Design and Technology*, Wiley-Interscience, Hoboken, NJ, USA, 2002.
- [7] F. D. Bannon, J. R. Clark, and C.T.-C. Nguyen, "High-Q HF Micromechanical Filters", *IEEE Journal of Solid-State Circuits*, vol. 35, no. 4, pp. 512-557, April 2000.
- [8] K. Wang, A-C. Wong, and C.T.-C. Nguyen, "VHF Free-Free beam High-Q Micromechanical Resonators", *IEEE Journal of MicroElectroMechanical Systems*, vol. 9, no. 3, pp. 347-360, September 2000.
- [9] M. A. Abdelmoneum, M. U. Demirci, and C.T.-C. Nguyen, "Stemless wine glass-mode disk micromechanical resonators", *Proceedings of IEEE Int. Conf. Micro-Electro-Mechanical Systems*, Kyoto, Japan , 2003, pp. 698-701.
- [10] C.T.-C. Nguyen, "Micromechanical Resonators for Oscillators and Filters", *IEEE International Ultrasonic Symposium*, vol. 1, pp. 489-499, 7-10 November 1995.
- [11] C.T.-C. Nguyen, "Frequency-Selective MEMS for Miniaturized Communication Devices", *Proceedings of IEEE Aerospace Conference*, pp. 445-460. March 1998.
- [12] J. Wang, J. E. Butler, T. Feygelson, and C.T.-C. Nguyen, "1.51-GHz nanocrystalline diamond micromechanical disk resonator with materialmismatched isolating support", *Proceedings of IEEE Int. Conf. Micro-Electro-Mechanical-Systems*, Maastricht, 2004, pp. 641-644.

- [13] G. Piazza, “MEMS Resonators for Frequency Control and Sensing Applications”, University of Pennsylvania, Philadelphia, 2010.
- [14] C.T-C. Nguyen, “MEMS Technology for Timing and Frequency Control”, *IEEE Transactions on Ultrasonics, Ferroelectrics, and Frequency Control*, vol. 54, no. 2, February 2007
- [15] Y. W. Lin, S. Lee, S.S Li, “Series-Resonant VHF Micromechanical Resonator Reference Oscillators”, *IEEE Journal of Solid-State Circuits*, vol. 39, no. 12, December 2004
- [16] W. N. Sharpe,, “Mechanical properties of MEMS materials”, *Semiconductor Device Research Symposium*, Washington, DC, USA, 2001, pp. 416-417.
- [17] M. Madou, *Fundamentals of Microfabrication*, CRC press, 1997.
- [18] M. Esashi, *Silicon Bulk Micromachining*, New Industry Creation Hatchery Center, Tohoku University, 2000.
- [19] S. Bart et. al., “Design Rules for a Reliable Surface Micromachined IC Sensor”, *IEEE Transactions on Ultrasonics, Ferroelectrics, and Frequency Control*, Vol. 54, No. 2, February 2007
- [20] MEMSCAP Inc, *PolyMUMPs Design Handbook*, Version 12.
- [21] University of Waterloo, *UW-MEMS Design Handbook*, Version 4.0,
- [22] M. Motiee, “MEMS IF/RF Filters”, *Master’s Thesis*, Department of Mechanical Engineering, University of Waterloo, 2003
- [23] W. T. Hsu, J.R. Clark, and C.T.-C. Nguyen, “Q-optimized lateral free-free beam micromechanical resonators”, *IEEE Solid-State Sensors and Actuators*, pp. 1110-1113, June 2001.
- [24] A. T. Ferguson, V.T. Nagarajb, “Modeling and design of composite free–free beam piezoelectric resonators”, *Sensors and Actuators A: Physical*, Issues 118, August 2005, pp. 223-231.
- [25] D. H. S. Maithripala, B. D. Kawade, J. M. Berg, “Applications of MEMS in Telecommunications”, *Canadian Workshop on MEMS/Micromachining: Apply MEMS Research in Canada*, Ottawa, Ontario, Canada, August, 2001.
- [26] L. Meirovitch, *Elements of Vibration Analysis*, McGraw-Hill, New York, 2<sup>nd</sup> edition, 1975.

- [27] W.T. Thomson, *Theory of Vibration with Applications*, Englewood Cliffs, NJ: Prentice-Hall, 1981.
- [28] A. Prak, M. Elwenspoek, and H. J. Fluitman, “Selective Mode Excitation and Detection of Micromachined Resonators”, *Journal of Microelectromechanical Systems*, vol. 1, no. 4, pp. 179-186, December 1992.
- [29] M. Konno, S. Oyama, “Equivalent Electrical Networks for Transversely Vibrating Bars and Their Applications”, *IEEE Transactions on Sonics and Ultrasonics*, vol. SU-26, no. 3, pp. 1140-1152, May 1979.
- [30] H. A. Tilmans, “Equivalent Circuit Representation of Electromechanical Transducers: I. Lumped-Parameter Systems”, *Journal of Micromechanics and Microengineering*, vol. 6, no. 1, pp. 157-176, March 1996.
- [31] H. A. Tilmans, “Equivalent Circuit Representation of Electromechanical Transducers: II. Distributed-Parameter Systems”, *Journal of Micromechanics and Microengineering*, vol. 7, no. 4, pp. 285-309, December 1997.
- [32] M. Motiee, R. R Mansour, “Novel MEMS filters for on-chip transceiver architecture, modeling and experiments”, *Journal of Micromechanics and Microengineering*, 2006, vol. 16, no.4, pp. 407-418.
- [33] J. H. Harlow, *Electric power transformer engineering*, CRC Press, 2005 pp. 2–216.
- [34] L. P. Huelsman, *Basic Circuit Theory*, Prentice Hall, Englewood Cliffs, NJ, 2 edition, 1984.
- [35] Agilent Technologies HP Advanced Design System (ADS) Software, <http://www.agilent.com>
- [36] S. Moaveni, *Finite Element Analysis*, 2<sup>nd</sup> edition, Pearson Education, 2003
- [37] COMSOL Multiphysics 4.2a, “MEMS Module Model Library”, <http://www.comsol.com>
- [38] Veeco Instruments Inc, “Wyko Optical Profiler User Quick Start Guide”, 2008, <http://www.veeco.com>
- [39] C.T.-C. Ngyen, “Transceiver Front-end Architecture Using Vibrating Micromechanical Signal Processors”, in *Topical Meeting on Silicon Monolithic Integrated Circuits*, pp. 23-32. IEEE, September 2001.

## APPENDIX A COMSOL Multiphysics Steps

The following steps are followed to perform the modal, static and dynamic analysis using COMSOL Multiphysics 4.2a.

### MODAL ANALYSIS

1. Enter COMSOL 4.2a in the Model Wizard to select **3D Geometry** from Space dimension list then click **next**.
2. In the Add physics tree, select Structural Mechanics > Electromechanics(emi) and then click **next**.
3. In the Studies tree, select Preset Studies > Eigenfrequency and then click **finish**.
4. In the Model Builder window, go to the setting window for Geometry, chose **µm** in the Units section.
5. Right click Model 1>Geometry to define the dimensions of the resonator beam.
6. Add materials to the model by right click Model 1> Materials and choose **Open Material Browser**.
7. In the Materials tree, select MEMS>Metal>Au or Poly-silicon and right click to choose **Add Material to Model** from the menu.
8. Modify the default mesh settings. In the Model Builder window, right-click Model 1>Mesh 1>Size.
9. Locate the Element Size section, click the **Custom** button. In the Element Size Parameters section, select **Extreme Fine**. Click the **Build All** button.
10. In the Model Builder window, click Step 1: **Eigenfrequency**, locate the Study Setting section, type **3** in the Desired number of eigenfrequencies edit field.
11. Right-click the Study setting window and choose **Show Default Solver**, click the **Compute** button.

12. Data sets. In the Model Builder window, expand the Results>Data Sets node, then click **Solution**.
13. Go to the Settings window for Solution. From the Frame list, choose **Material (X, Y, Z)**.
14. In the Model Builder window, right click Results>3D Plot Group and choose **Surface**.
15. Go to the Settings window for Surface, right-click and choose **Deformation**. Locate the Expression section. In the X component edit field, type **u**. In the Y component edit field, type **v**. Click the **Plot** button.

## STATIC ANALYSIS

1. Follow the steps from 1 to 4 in modal analysis.
2. Define the dimensions of the resonator with support structures, anchors and bottom electrode in Geometry setting window.
3. Build an air box around the resonator structure in Geometry.
4. Add materials to the model by right click Model 1> Materials and choose **Open Material Browser**.
5. In the Materials tree, select MEMS>Metal>Au or Poly-silicon and right click to choose Add Material to Model>domain 1 (Resonator structure) from the menu.
6. Select Built-in>Air and right click to choose Add Material to Model>domain 2 (Around air).
7. Set up the solid mechanics and electrostatics boundary conditions. In the Model Builder window, right-click Model 1>Electromechanics and choose **Linear Elastic Material Model**.
8. Go to the Domain setting section. From the Selection list, apply a **fixed constraint** on the base of the resonator electrodes.
9. Right-click **Electromechanics** and choose the boundary condition

- Structural>Fixed Constraint, select the surface of electrode.
10. Use a fixed mesh in the solid dielectric domains that are assumed to be rigid. Right-click **Electromechanics** and choose the domain setting Deformed Mesh>Fixed Mesh. Select domain electrode and anchors.
  11. Apply electric potential boundary conditions on grounded surfaces. Right-click Electromechanics and choose **Electric Potential**.
  12. Go to the Settings window for Electric Potential. Locate the Boundary Selection section. From the Selection list, choose **electrode boundaries**. In the  $V_0$  edit field, type **25 V**.
  13. Go to the Settings window for Electric Potential. Set the  $V_0$  of resonator boundaries as **0 V**.
  14. Mesh the model following the same steps 7 and 8 as in modal analysis.
  15. In the Model Builder window, right-click Study 1 and choose **Compute**.
  16. Plot the Z-displacement of the structure. In the Model Builder window, right-click Results>Displacement (emi)>2D Plot Group>Surface.
  17. Go to the Settings window for Surface. Locate the Expression section. In the Expression edit field, type **v**. Click the **Plot** button.
  18. Create a plot to show the electric potential contours in the gap. Locate the Expression section. In the Expression edit field, type **V**. In the Total levels edit field, type **10**. Click the **Plot** button.

## DYNAMIC ANALYSIS

1. Follow the steps from 1 to 13 in static analysis.
2. Add a harmonic perturbation to the DC bias term, to represent the offset AC drive voltage. Right-click Electric Potential and choose **Harmonic Perturbation**.
3. Go to the Settings window for Harmonic Perturbation. Locate the Electric Potential section. In the  $V_0$  edit field, type **0.1**

4. Set up the frequency domain study. In the Model Builder window, right-click Resonator\_3d.mph and choose **Add Study**.
5. Go to the Model Wizard window. Find the Studies subsection. In the tree, select Preset Studies>Prestressed Analysis, Frequency Domain. Click **Finish**.
6. In the Model Builder window, click Step 2: Frequency-Domain, Perturbation. Locate the Study Settings section. In the Frequencies edit field, type range **(245[kHz], 1[kHz], 275[kHz])**.
7. Go to the Study Settings section. Clear the Generate default plots check box. Click the **Compute** button.
8. Produce a plot of the frequency response of the system. In the Model Builder window, right-click **Results** and choose **1D Plot Group**.
9. Go to the Settings window for 1D Plot Group. From the Data set list, choose Solution 2. Right-click 1D Plot Group 4 and choose **Point Graph**. Select the midpoint of the beam only.
10. Go to the Settings window for Point Graph. Locate the y-Axis Data section. In the Expression edit field, type **v**. Click the **Plot** button.

## APPENDIX B PolyMUMPs Static Measurements

Included in this Appendix are screen-shots of the static measurement for the 49.4  $\mu\text{m}$  free-free beam PolyMUMPs resonator.

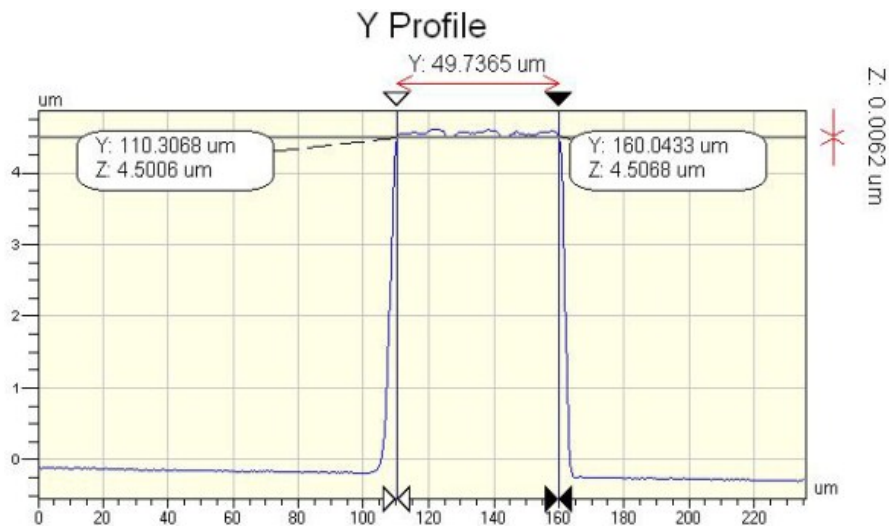


Figure B. 12: 2D surface profile along the length of the PolyMUMPs resonator

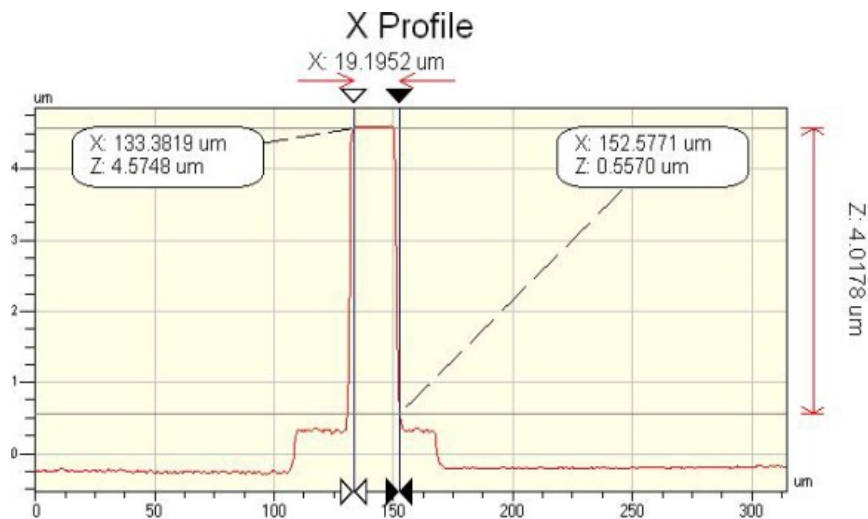


Figure B. 12: 2D surface profile along the width of the PolyMUMPs resonator

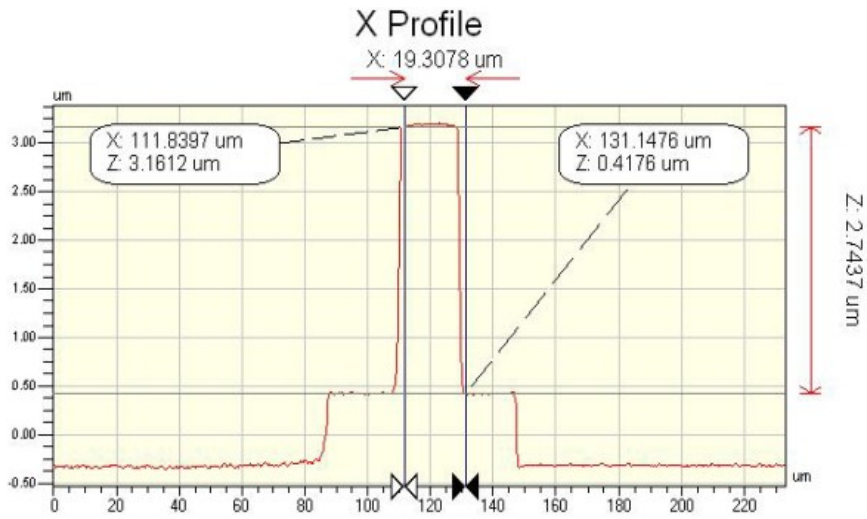


Figure B. 13: X Profile of the PolyMUMPs resonator after applied voltage

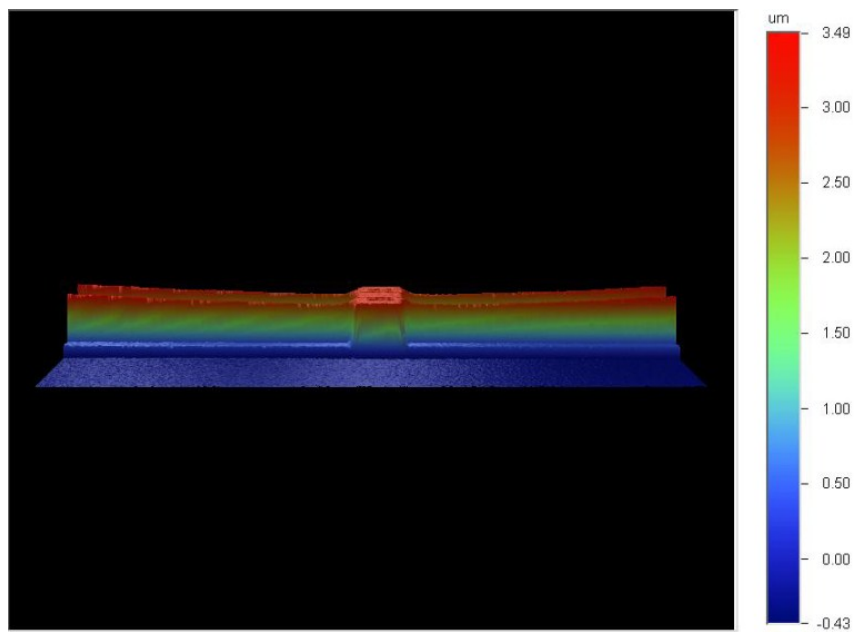


Figure B. 14: 3D side view of the micro-resonator